

Determining the effective temperature of cool stars from near-infrared spectra

Henrik Rhodin

Lund Observatory
Lund University



2015-EXA92

Degree project of 60 higher education credits (for a degree of Master)
May 2015

Supervisor: Nils Ryde
Co-supervisors: Hampus Nilsson and Henrik Hartman

Lund Observatory
Box 43
SE-221 00 Lund
Sweden

Abstract

Context. Effective temperature is one of the fundamental stellar parameters. A traditional spectroscopic way to determine it is from optical spectra using excitation balance of Fe-lines. With technological advances and the advent of the next generation telescopes there will be an emphasis on the relatively unexplored near-IR (NIR) wavelength region (1-5 μm). A method to determine the effective temperature based on NIR spectra is needed.

Aims. In a proactive attempt, this thesis explores the NIR for the potential of such a method. Reference iron-linelist are created and optimised for the determination of stellar parameters of cool stars (mainly giants). The K-giant benchmark star, Arcturus (α -Boo), is used as a testbed for the analysis.

Methods. An IDL script is written to select Fe-lines for stellar parameter diagnostics, with constraints based on blend-percentage and line-strength. Empirical line-strengths (astrophysical gf-values) of evaluated Fe-lines are solved against the solar spectrum using 1D-LTE MARCS model atmospheres and VALD to define atomic data. These are used as input to generate synthetic spectra of Arcturus which are confronted with high-resolution observations. The final Fe-linelist are used to retrieve the fundamental stellar parameters of Arcturus using SME for spectrum synthesis.

Results. The derived gf-values follow a one-to-one correspondence with the available laboratory measurements. Theoretically calculated values show a larger spread, indicative of configuration interaction and level-mixing. With an independently determined surface gravity, the effective temperature of Arcturus can be retrieved using ~ 20 lines to a precision of ± 50 K. The Fe-linelist constructed for the J- and H-bands each span excitation potentials of the same range as those constructed for the optical spectral region used in other studies.

Conclusions. The results indicate that the NIR has a large potential for the determination of effective temperature and metallicity. The absence of observed Fe II lines suggests that surface gravity must be determined by an independent method, or alternatively using pressure-sensitive wings of strong lines in other atomic species.

Acknowledgements

Above all, I would like to express my deepest gratitude to Nils Ryde, Henrik Hartman and Hampus Nilsson for supervising me in this endeavour. It has been a rewarding experience. The energy and time you have invested in answering every detailed question that I've had is unparalleled. You have been encouraging in times of need and a source of inspiration throughout this thesis. The three of you have my deepest appreciation.

I would also like to say thank you Gregory Ruchti for valuable feedback concerning the science and structure of the official draft thesis and to Ross Church for comments on language and English grammar. Lastly, I would like to thank Henrik Jönsson for advice and for sharing your results; my fellow office mates for a good working atmosphere; and Asli Pehlivan for all your support and patience.

Populärvetenskaplig beskrivning

När vi tittar upp mot himlen kan vi urskilja skenet från tusentals strålande stjärnor. En mörk natt kan man också förnimma ett ljussvagt stråk som spänner över himlen; *Vintergatan*. Stråket består av (för ögat) oupplösta stjärnor, som tillsammans med gas och stoft sammanfogats under gravitationens inverkan för att, över tid, bilda vår hemgalax. Tittar man med ett teleskop kan man se en enorm variation och rikedom av galaxer - allt från spiraler och bargalaxer till sferoider. Hur denna morfologiska fauna uppstått är en fråga som kvarstår, vilket gjort galaxbildning- och utveckling till ett hett ämne inom forskningen. För att bygga upp en enhetlig bild detaljstuderar man galaxers grundläggande beståndsdelar; *stjärnorna*. Stjärnor med olika åldrar utgör ”ögonblicksbilder” som kan sammanfogas till en förståelse av galaxernas temporala utveckling. Stjärnor med olika sammansättning kan sammanfogas till ämnesgradienter som ger en indikation på galaxers spatiala uppbyggnad.

Ljuset som en stjärna utstrålar beror på de rådande förhållandena i stjärnatmosfären; däribland *temperaturen*, *trycket* och den *kemiska sammansättningen*. Genom att studera en stjärnas slutgiltiga spektrum kan vi därför dra slutsatser om de förhållanden som karakteriserar stjärnan. Ett stjärnspektrum skapas när ljus växelverkar med materien, och består av absorptions- och emissionslinjer vars positioner (våglängder) motsvarar atomära övergångar från exciterade tillstånd. Ett stjärnspektrum blir stjärnans ”streckkod”, och genom att läsa av streckkoden kan man bilda sig en uppfattning om stjärnans struktur och sammansättning. För att läsa av streckkoden brukar man använda sig av synligt ljus. Dessvärre har synligt ljus en tendens att interagera med gas och stoft längs vägen till observatören vilket kan filtrera ut delar av ljuset. Detta resulterar i att (i) ljusstyrkan från stjärnan minskar vilket försvårar avläsningen av spektrumet (streckkoden), och (ii) det slutgiltiga spektrumet inte längre är stjärnans eget utan en sammansättning av allt som ljuset interagerat med på vägen.

I denna avhandling har jag undersökt möjligheten att bestämma temperaturen med hjälp av infrarött ljus, vilket inte är lika känsligt. Jag har studerat *vilken* bit och *hur stor* bit av stjärnans streckkod som behövs, och har på så sätt lyckats konstruera en stjärntermometer. Detta har gjorts med hjälp av noga utvalda järnövergångar som visat sig vara särskilt temperaturkänsliga. Av resultaten framgår att man inte behöver stjärnans hela streckkod utan väljer man en liten bit av streckkoden med hänsyn till de rådande förhållandena kan stjärnans temperatur bestämmas entydigt.

Contents

1	Introduction	5
2	Framework	8
2.1	Spectrum Synthesis	8
2.2	Validating 1-D	12
2.3	Validating LTE	13
3	Method	16
3.1	Evaluating Blends	17
3.2	Astrophysical gf-values	22
3.3	Data Analysis	25
3.4	Retrieving Stellar Parameters	33
4	Results	37
4.1	Retrieval of Solar Parameters	37
4.2	Arcturus-optimised Fe-linelist	39
4.3	Arcturus Stellar Parameters	47
4.4	Uncertainties in Teff	51
5	Conclusion	57
5.1	Summary	57
5.2	Future Prospects	58
A	Astrophysical gf-values	63
B	SME Jobs for Temperature Uncertainties	79

List of Figures

3.1	A flow-chart depicting the major steps in the procedure. The figure should be interpreted following the arrows that connect two consecutive steps, starting from top left. Parenthesised abbreviations denote the scripts constructed and software packages used.	16
3.2	Schematic overview of a constructed Region of Interest (ROI). The green curve represents the composite spectral feature as it would appear in a spectral analysis. It consists of the Fe-line of interest (black), an unresolved blend (blue) and an outlier (red) whose strong wing influences the total ROI equivalent width.	20
3.3	Synthetic spectra (blue) do not reproduce observed spectra (black), resulting from incorrect atomic data. Yellow regions represent line-masks. In (a) and (b) this is caused by errors and uncertainties in the gf-values of known transitions or gf-values assigned to wrongly identified transitions. In (c) the absence of atomic data prevents the observed spectral feature from being reproduced. In (d) a correct gf-value has been assigned to the wrong transition, or the energy levels associated with the line have not converged in atomic structure calculations.	22
3.4	A strong hydrogen transition with broad Lorentzian wings exerting influence on the local continuum placement of other lines in its vicinity. The synthetic spectrum is depicted in blue, the observed spectrum in black. Yellow regions represent line-masks. This can cause the gf-value (or equivalently the abundance) of iron, as determined based on the Fe I transitions $\lambda 12807.152\text{\AA}$ and $\lambda 12808.243\text{\AA}$ to be seriously off, if not dealt with on a line-by-line basis. To minimise the resulting effect on the stellar parameters, such problematic transitions were avoided in the analysis.	23
3.5	Optimised gf-values, solved using an inverted analysis of solar H-band observations. The synthetic spectrum is depicted in blue, the observed spectrum in black. The faint- and dark yellow regions represent continuum- and line-masks. For the sake of clarity, a spectral segment with low noise and an absence of telluric lines and molecular features is used. .	24
3.6	Partial Fe I energy-level diagram in terms of χ_{exc} , grouped according to configuration and parent term (based on the J- and H-band solar spectra). Black lines indicate levels with at least one transition whose assigned literature gf-value is in agreement with that of this work, whilst red lines indicate levels without gf-values in agreement. The discriminator is chosen to be at a gf-value giving a difference of $\pm 25\%$ yield in abundance. The dashed horizontal line at 7.9 eV indicates the ionisation energy of Fe I. Boxes trace the energy interval for all levels of a given nl -symmetry. The dotted lines connect boxes of the same nl -symmetry belonging to different parent-terms for a given configuration.	26

3.7	Comparison between astrophysical (this work) oscillator strengths (gf-values) and experimental gf-values where such exist. Blue dots represent values determined by Ruffoni et al. (2013), whilst red triangles represent values measured by O'Brian et al. (1991). The black dotted line represents a theoretical one-to-one correspondance. The blue line is a linear fit through the data points. Typical experimental uncertainties are of the order 0.09 dex, too small to be depicted meaningfully.	29
3.8	Comparison between this works gf-values and those published in the VALD database, plotted as a function of this works gf-values. Dotted horisontal lines indicate differences in gf-values corresponding to $\pm 25\%$ yield in abundance. References are (Kurucz 2007); (Kurucz 2006); (Kurucz 1988); (Biemont et al. 1999); (Raassen & Uylings 1998); (no reference); (Kurucz & Peytremann 1975); and (O'Brian et al. 1991). Correspondingly, black triangles are the only data points based on experimental measurements.	31
3.9	A comparison between the gf-values of this work and those published in the VALD database, plotted as a function wavelength λ . References and figure nomenclature are as Figure 3.8.	31
3.10	A comparison between the gf-values of this work and those published in the VALD database, plotted as a function excitation potential (eV). References and figure nomenclature are as Figure 3.8.	32
3.11	A comparison between the gf-values of this work and those published in the VALD database, plotted as a function of the proxy for equivalent width, as given by Eq. 3.5. The data points have been offset horizontally by adding a constant to avoid clumping towards the lower equivalent width limit. References and figure nomenclature are as Figure 3.8.	32
3.12	Comparison of an Arcturus summer- and winter spectral segment (upper and lower panel respectively), plotted as a function of wavenumber. The segment corresponds to the wavelength-region around $\lambda\lambda$ 1.64- 1.65 μm . The red and blue curves denotes the telluric and stellar spectra respectively, and the dotted line denotes a continuum normalisation to unity. The telluric lines have a fixed position because they arise in the rest-frame of the observer whilst the orbital motion of the Earth causes shifts in the stellar features (red) as observed at different times.	34
4.1	Histograms comparing the distribution of equivalent widths for Fe-linelist fulfilling different thresholds on the imposed blend-criteria (30% (blue), 20%(red), 5%(yellow)). Note that the vertical axis in (a) and (b) have different scales.	39
4.2	Histograms comparing the distribution of excitation potentials, χ_{exc} , for Fe-linelist fulfilling different thresholds on the imposed blend-criteria (30% (blue), 20%(red), 5%(yellow)). Note that the vertical axis in (a) and (b) have different scales.	40
4.3	Histograms comparing the distribution of excitation potentials, χ_{exc} , in the J- and H band Fe-linelist of this work with Jönsson's (2014) optical linelist based on a similar method. The J- and H band Fe-linelist plotted allow for 30% blends, the large blend being selected as the threshold values of Jönsson (2014) were not known. Note that the vertical axis in comparisson with the J-band (a) and H-band (b) have different scales.	41

List of Tables

3.1	α -Boo Molecular Species	21
3.2	Literature Values Statistically Compared	27
4.1	Recommended Fe-linelist for the J-band.	43
4.2	Fe-linelist for the H-band, work in progress.	44
4.3	Arcturus Stellar Parameters, H-band.	49
4.4	Arcturus Stellar Parameters, J-band.	50
4.5	Temperature differences induced by line-mask placement. ΔT and σ are calculated based on N=4 measurements.	53
4.6	Temperature differences induced by continuum-mask placement. ΔT and σ are calculated based on N=4 measurements.	53
4.7	Temperature differences induced by gaussian-distributed uncertainties in gf-values assuming $1\sigma = 0.02$, with ΔT and σ calculated based on N = 21 measurements.	55
A.1	Astrophysical gf-values	63
B.1	Temperature-measurements for the different linelists obtained when adding Gaussian noise in gf-values assuming a standard deviation of $\sigma = 0.02$ dex.	79

Chapter 1

Introduction

At present, a good near-infrared (NIR) baseline of iron (Fe) transitions for stellar diagnostics does not exist. In response, this master thesis aims to create and evaluate a general reference Fe-linelist to determine the effective temperature, T_{eff} , and the metallicity, $[\text{Fe}/\text{H}]$, of cool stars using NIR high-resolution spectra. Together with surface gravity, $\log(g)$, and in the case of 1D-spectral synthesis the *microturbulence*, ξ_{mic} , these are the fundamental stellar parameters that govern the shape of the spectral energy distribution (SED) and determine the structure of the star's atmosphere. This thesis will investigate how spectral bands, the number of transitions, the span in excitation potential and how atomic- and molecular blends influence the determined values of the stellar parameters.

Where atomic data is missing, empirical line-strengths (astrophysical gf-values) will be determined against the solar spectrum. Ensuring that the solar parameters can be retrieved with the updated values, an Fe-linelist will be constructed and optimised to Arcturus (α -Boo), - a K-giant benchmark star with stellar parameters $T_{\text{eff}} = 4268\text{K}$, $\log(g)=1.66$, $[\text{Fe}/\text{H}] = -0.52$ (Ramírez & Allende Prieto 2011), which will act as a testbed for the study. The linelist will be used to determine level populations, excitation and ionisation equilibria, from which the synthetic spectra created are iteratively matched to observations according to a χ^2 -minimisation routine. This, and the assumption of iron as a proxy for metallicity, allows the fundamental stellar parameters to be determined.

The motive behind the thesis is an increased emphasis in the NIR spectral region from the *scientific* and *technological* communities alike. Research on galaxy formation and evolution require precise stellar parameters to resolve abundance gradients in stellar populations. These can be combined with dynamical information to reconstruct the galactic history. The optical spectral region is successfully used for spectral analysis; eg. the Gaia-ESO Survey (Gilmore et al. 2012; Hourihane et al. 2014), but becomes problematic for the study of stars in obscured fields (e.g. the Galactic bulge) and over large distances since interstellar dust causes extinction which reduces the signal-to-noise, thereby preventing high-resolution studies. Whilst the effect of extinction *decreases* with wavelength, the stellar flux rapidly drops off with the Rayleigh-Jeans tail of the Planck-function. The NIR

represents a middle-ground, which for intrinsically luminous, cool sources is able to mitigate the effect of high extinction and low photon counts alike.

The advantage of the NIR for detailed spectroscopic studies has been recognised by various studies, including Ryde & Schultheis (2015) and the APOGEE consortium (Smith et al. 2013; Holtzman et al. 2015) who are attempting to improve our understanding of the galactic evolution and chemical history of the Milky Way. This has driven the quest of obtaining reliable atomic data also in the NIR (Ruffoni et al. 2013; Ruffoni et al. 2014).

With emerging cross-dispersed NIR spectrographs like 'CRIRES+' on board the *Very Large Telescope* (VLT); 'GIANO' on the *Telescopio Nazionale Galileo* (TNG); the 'IGRINS' instrument at the *McDonald Observatory*; and the advent of the next generation European flagship telescope, the *European Extremely Large Telescope*, (E-ELT) with its 'SIMPLE' instrument, the capacity of sampling full spectral bands in single exposures at high spectral resolution will be met (Oliva et al. 2014; Origlia et al. 2014; Oh et al. 2010; Origlia et al. 2013, respectively). Combined with adaptive optics (AO) which is optimised for the NIR, and improved infrared detectors (currently being built), this will push the frontier of what is observationally possible from a technological standpoint, allowing ground-based spectroscopic studies using the J, H, K, L and M atmospheric transmission bands.

We are thus at a stage where there are scientific and technological interests that drive astrophysical endeavours also towards the NIR. In the context of spectral analysis, there will be a demand for a corresponding method for NIR-spectroscopy based on the same principles as that of optical-spectroscopy. In a proactive attempt, this thesis intends to explore the NIR for the possibility of such a methodology.

The thesis is structured as follows; Chapter 2 presents the scientific framework required to understand the following sections. Chapter 3 describes the methods of procedure, and Chapter 4 presents the acquired results with related discussions. Chapter 5 provides a summary with conclusions and future prospects.

Chapter 2

Framework

This chapter intends to explain the underlying framework, with an emphasis on its possibilities and limitations for cool Arcturus-like giants. Section 2.1 outlines the principles of *spectrum synthesis*, with emphasis on the SME software package, the MARCS model stellar atmospheres and the VALD atomic line database. The analysis of cool stars meets two main difficulties; they have sub-surface convection and a strong radiation field in their photospheres making the implicit assumptions behind SME and MARCS questionable. Section 2.2 and Section 2.3 discuss the validity of these assumptions, namely that of 1-Dimensionality (1-D) as opposed to 3-D radiative hydrodynamic (3-D RHD) models and *local thermodynamic equilibrium* (LTE) as opposed to *non-LTE* (NLTE) in the context of the cool giants.

2.1 Spectrum Synthesis

The extraction of fundamental stellar parameters from an empirical spectrum is challenging, and relies on inference from spectral features. Moreover, it necessarily includes simplifications to treat complicated physical processes (e.g. convection) and computational limitations (e.g. geometry of the problem; boundary conditions).

Spectroscopically, inference can be used in two ways; by *equivalent width measurements* and/or *synthetic spectra*. This thesis uses the Uppsala codes 'BSYN' and 'EQWIDTH'-based on routines from the MARCS model atmosphere code (Gustafsson et al. 2008) - for the former, and 'Spectroscopy Made Easy' (SME, Valenti & Piskunov 1996) for the latter. The advantage of equivalent widths is that they allow comparison of the strength of spectral features, independent of the line profiles. This is particularly useful for low-resolution analysis where the instrumental profile dominates intrinsic line profiles; but suffers drawbacks of (i) *being vulnerable to atomic and molecular blends hidden beneath the profile*; and (ii) *being without quality-checks such as visual inspection and/or without a measure of the goodness of fit* which complicates the inference of stellar parameters. High-resolution spectroscopy takes advantage of the intrinsic line-profiles which can be resolved and convey

additional information regarding stellar rotation ($v \sin i$) and velocity fields.

Spectrum synthesis numerically computes radiative transfer through a physical structure, e.g. a stellar atmosphere. SME uses MARCS 1D-LTE model atmospheres in hydrostatic equilibrium (Gustafsson et al. 2008) assuming standard α -enhancement, which together with the fundamental stellar parameters (T_{eff} , $\log(g)$, $[\text{Fe}/\text{H}]^1$), and convection parametrised in terms of *microturbulence* (ξ_{mic}) using Mixing-length theory (Henyey et al. 1965) define the radial stratification of the structure. MARCS models assume plane-parallel geometries for solar-like stars and dwarfs, whilst giants with their extended atmospheres are treated using spherical geometries. Combined with line data, radiative transfer through the structure produces continuous and line opacities of the elements in it. SME accepts line data in the format returned by the Vienna Atomic Line Database (VALD) (Piskunov et al. 1995; Heiter et al. 2008; Kupka et al. 1999). Line opacities are calculated assuming Voigt profiles for all elements apart from Hydrogen (Valenti et al. 2012). Due to their complex behaviour, Hydrogen profiles are computed using the code 'HLINOP' which accounts for self-broadening; a van der Waals-type interaction in which hydrogen absorbers are perturbed by other hydrogen atoms (Barklem & Piskunov 2003).

The solution to the radiative transfer equation requires a *source function* to quantify the contribution of emission- and absorption processes of the local medium to the emergent intensity. The source function must satisfy flux consistency at every depth of the atmosphere.² Being a function of the physical structure, the source function is solved iteratively by developing the stellar parameters according to a Levenberg-Marquet (LM) algorithm. This uses a gradient search of the χ^2 -plane to step forward in the minimisation procedure. SME assumes that particle collisions control the energy partitioning of matter; *local thermodynamic equilibrium* (LTE). This means that the *material* energy distributions (velocity, excitation, ionisation) are fixed by the local kinetic temperature (following the Maxwell, Saha and Boltzmann distributions respectively), whilst the *radiative* energy distribution obeys the Planck function. Under such conditions, radiative transfer reduces to finding the temperature structure of the atmosphere.

¹The *metallicity* of a star is a measure of the fraction of its atmospheric iron to hydrogen, normalised against the Sun:

$$[\text{Fe}/\text{H}]_{\star} = \log_{10} \left(\frac{N_{\text{Fe}}}{N_{\text{H}}} \right)_{\star} - \log_{10} \left(\frac{N_{\text{Fe}}}{N_{\text{H}}} \right)_{\odot},$$

where N denotes the number density of atoms belonging to the element indicated by the subscripts, \star refers to the star, and \odot refers to the Sun.

²Formulated in terms of the *energy equilibrium equation* which states that $\mathcal{F}_{\text{conv}} + \mathcal{F}_{\text{rad}} = \frac{\mathcal{L}}{(4\pi r^2)}$, where the first and second term of the left hand side denote flux contribution from convection and radiation respectively, and \mathcal{L} is the stellar luminosity. The condition is iteratively solved by requiring that $\frac{d}{dr}((\mathcal{F}_{\text{conv}} + \mathcal{F}_{\text{rad}})r^2) = 0$. For $\mathcal{F}_{\text{conv}} = 0$ the condition for radiative equilibrium is retrieved. This is often the case in the upper layers of the models.

Although collisions govern the rates, it is the presence of radiative transitions which cause opacity and hence allow the formation of stellar continua (bound-free and free-free transitions) and spectral features (bound-bound transitions). The question is: Do spectroscopic measurements reflect the *true/total* elemental abundance or trace the fractional abundance responsible for the radiation? The answer is subtle; although collisions maintain the partitioning of the level populations, the spectroscopic measurement is proportional to the level population and thus to the partitioning. It is this built-in coupling that implies a measure of the *true* abundance.

Although the complexity is reduced by assuming LTE the iterative procedure is computationally expensive, especially when one has to cover a large stellar-parameter-space. To circumvent this issue, SME interpolates over a precomputed library of MARCS atmospheric structures. The interpolated atmosphere is then propagated through a radiative transfer calculation to give an intensity spectrum at different limb angles. These are integrated over the stellar disc to give a flux spectrum. A continuum-normalised flux spectrum is convolved with an instrumental profile to match the spectral resolution of the instrument; and with Gaussian profiles to account for macroturbulence (v_{mac}) and rotational broadening ($v \sin i$).

Somewhat simplified, the observed spectral line consists of an intrinsic strength and shape which is characterised by the conditions *during* "line-formation", (affecting strength and profile alike³); and "post-line-formation" modifications (affecting the profile only). Referring to these two stages as W and φ respectively, a spectral line, ϕ_λ , can be modelled as

$$\phi_\lambda(\theta_\star, \alpha, R, v \sin i, v_{\text{rad}}) = W_\lambda(\theta_\star, \alpha^l, \alpha^c) * \varphi_\lambda^{\text{inst}}(R) * \varphi_\lambda^{\text{rot}}(v \sin i) * \varphi_\lambda^{\text{mac}}(\theta_\star), \quad (2.1)$$

where $\theta_\star = [\text{Teff}, \log g, [\text{Fe}/\text{H}], \xi_{\text{mic}}]$ denotes the stellar parameters, α denotes line (l) and continuum (c) opacities, $R = \lambda/\Delta\lambda$ denotes the resolution of the instrument, $v \sin i$ characterises the broadening by the (projected) stellar rotation. The convolved spectrum is wavelength-shifted by a factor characterised by v_{rad} to account for the doppler shift caused by the stellar motion (relative to Earth) through space.

SME employs a direct pixel-by-pixel comparison between the synthetic spectrum and the empirical spectrum to evaluate the fit and retrieve the stellar parameters. The fit minimises a reduced χ^2 -statistic weighted by the observed spectral flux over pre-masked data-segments,

$$\chi^2(\theta_{\text{free}}) = \frac{1}{N - \theta_{\text{free}} - \gamma} \sum_{i=1}^N \left(\frac{S_i^{\text{obs}} - S^{\text{synt}}(\lambda_i | \theta_{\text{free}})}{\sigma_i} \right)^2, \quad (2.2)$$

where S_i^{obs} is the observed flux, S^{synt} is the synthetic flux at wavelength λ_i assuming global free parameters θ_{free} , N is the number of masked data-points, γ is the number of masks

³The strength implicitly including *natural*-, *thermal*- and *pressure* broadening which are convolved to give the characteristic *Voigt-profile*.

and σ_i is the uncertainty in the observed spectrum points.

The minimisation varies pre-selected "free parameters", normally taken to be θ_* (or a subset of θ_*), but can also include line parameters, radial velocity, instrumental broadening and continuum level. By masking carefully selected spectral lines sensitive to θ_{free} , the stellar parameters can be retrieved. This method relies on the excitation-ionisation balance of iron lines. T_{eff} is determined by requiring an elemental abundance to be independent of excitation potential.⁴ Implementation-wise, this is solved by minimising the resulting slope; a large span in excitation potential acting as a lever to constrain the value. $\log(g)$ is determined by (i) forcing the abundance obtained from lines of different ionisation stages to be equal, or (ii) using the pressure-sensitive wings of strong lines. $[\text{Fe}/\text{H}]$ is retrieved directly as the output value of the χ^2 -minimisation. The value of ξ_{mic} is determined so that the elemental abundance is independent of line-strength. Since only strong lines are sensitive to it, the line-list requires transitions which span the range of equivalent widths.

It is important to emphasise that stellar parameters are not retrieved independently of each other. They are correlated, with degeneracies in the effect of each parameter on a spectral line, and are solved simultaneously. Further, it should be recognised that the χ^2 -value minimises the *difference* between the spectra but represents nothing physical in itself; an optimised fit does not necessarily entail physical information.

⁴Assuming the line belongs to the same ionisation stage and element (refer to Section 2.3 for a discussion regarding abundance departures caused by NLTE effects).

2.2 Validating 1-D

Rather than static balls of gas in hydrostatic equilibrium, stars are dynamic with turbulent flows, magnetic fields and convective motions in their envelopes (Nordlund et al. 2009). This has been observed *directly* in the form of convective cells and solar granulation, and *indirectly* using line bisectors which indicate the presence of asymmetrical velocity fields (slow steady up-flows separated by fast turbulent downdrafts) that influence line-formation (Nordlund & Dravins 1990). Such physics is 3D, time-dependent and non-local, and can have consequences on the atmospheric structure and the emergent radiation, both of which affect the stellar spectrum (Collet et al. 2007, 2011). This requires a 3D time-dependent hydrodynamic treatment, which naturally accounts for the interaction between radiative and convective energy transport. Since convection and turbulence are structure- and depth dependent, they cannot be accurately described with fixed-valued micro- and macro- turbulence in 1-D.

What then justifies the use of 1-D model atmospheres?

One of the major challenges is that a full time-dependent 3-D radiative-hydrodynamic (RHD) treatment of radiative and convective transport in stellar photospheres is computationally expensive. This is because one is required to compute several radiative ray directions for every convective time-step. Although it can be used to explore the validity range of 1-D hydrostatic model atmospheres, this computational limitation means that a 3D treatment cannot be produced over a large range of stellar parameters (Collet et al. 2007).

Hayek et al. (2011) showed that the line-strengths of high-excitation and ionized species are vulnerable to continuum scattering which raises the continuum at wavelengths of $\lambda < 4000$ Å in metal-poor giants. This can lead to line-strength desaturation, which causes large abundance corrections for strong lines in 3D, the corrections decreasing with low-excitation lines, longer wavelengths, and higher metallicity. Bergemann et al. (2012) showed that strong low-excitation ($\chi_{exc} < 2$ eV), Fe I lines are sensitive to the atmospheric structure, specifically for cool metal-poor stars. Although these effects manifest as departures from LTE (see Section 2.3), it was shown that they only appear in a 3D treatment. The reason is that convection acts to cool the outer layers, giving non-local radiation field a larger influence. This effect causes 1D hydrostatic models (both LTE and NLTE) to underestimate the effective temperatures when using excitation balance of Fe I lines (Ruchti et al. 2013). Arcturus, although cool, only has a slight sub-solar metallicity. For this reason, the effect on the resulting spectrum should be small. In light of the computational limitations, this should validate the use of 1-D model atmospheres for this thesis work.

2.3 Validating LTE

Cool M- and K giants have extended photospheres with extremely low densities. With decreased density, the photon mean-free path is extended, and radiation gradually decouples from matter. As the decoupling progresses, the radiation field departs from the Planck function and becomes *non-local* in character. Thus, ionisation- and excitation distributions are not set by the local temperature, but require a *non-local thermodynamic equilibrium* (NLTE) treatment to allow for the interaction of matter with a non-local radiation field.⁵ In fact, it seems as if any physical structure in hydrostatic equilibrium (such as a stellar atmosphere) would inevitably introduce a radial density-gradient, and would therefore be subject to NLTE effects.

What then warrants the use of LTE-based MARCS model atmospheres - especially with respect to cool giants with similar stellar parameters to Arcturus?

Whilst a NLTE treatment has a stronger physical foundation that incorporates all the (known) mechanisms for light-matter interaction, it suffers computational limitations. Emerging radiation depends on the level populations, which in themselves are a function of the incident radiation; thereby providing a coupling between the non-local radiation field and the local properties of the gas. A NLTE treatment requires the rate equations to be solved simultaneously with the radiative transfer equation for all relevant frequencies. This means that a NLTE treatment requires additional input data that is often uncertain and incomplete for radiative and collisional processes such as photo-ionisation cross-sections. A NLTE treatment can alter spectral line behaviour in different ways; it can affect equivalent widths (Lind et al. 2012), cause line-asymmetries (Asplund 2005), or leave the spectrum unchanged depending on the *strength* and *mechanism* responsible for the departure.

NLTE effects on elemental abundances are parametrised in terms of *departure coefficients* which quantify departures from LTE. Although the effects on spectral line formation are well understood for most chemical elements (Niemczura et al. 2014), there are numerous mechanisms that can be responsible for NLTE effects (resonance scattering, overionisation, photon pumping, photon suction, etc.). These may target specific levels, ionisation stages and/or elements, making it difficult to predict the spectral consequences *a priori*. Generally however, NLTE seems to preferentially act on low-excitation transitions (Asplund 2005), and seems to vary with line strength. The effects on strong lines ($W_\lambda > 60 \text{ m}\text{\AA}$) systematically increase with excitation potential (Bergemann et al. 2011), although later studies argue that strong low-excitation Fe I lines also appear sensitive to the atmospheric structure (Bergemann et al. 2012). Weak line ($W_\lambda < 60 \text{ m}\text{\AA}$) corrections, though observed to be independent on excitation potential, seem to be correlated with the line-formation depth (Bergemann et al. 2011).

⁵Whilst LTE is an *approximation*, NLTE is *not*.

Recent attempts to accurately quantify departures from LTE in a systematic way over a range of stellar parameters have been conducted. The results suggest that 1-D LTE excitation-ionisation balance of Fe lines introduce systematic biases in stellar parameters, the departures being especially severe and increasing with low metallicity and/or low surface-gravity giants. The departures are driven by over-ionisation of Fe I due to an excessive UV radiation field from the deep layers of the photosphere that cause a population depletion in Fe I levels whilst maintaining LTE values for Fe II levels (Bergemann et al. 2011; Mashonkina et al. 2011). However, for Arcturus parameter-space ($T_{\text{eff}} \sim 4250$ K, $[\text{Fe}/\text{H}] \sim -0.52$ dex, $\log(g) \sim 1.66$ dex), LTE and NLTE predictions seem to converge, with only small corrections to the effective temperature needed (Bergemann et al. 2012; Ruchti et al. 2013). Lind et al. (2012) constructed a grid tracing the departure coefficients as a function of stellar parameters, which for Arcturus predicts negligible departures from LTE.

All things considered, recent studies indicate that departures from LTE are negligible for Arcturus-like giants - especially in light of 3D effects and uncertainties involved with missing atomic data. The use of LTE MARCS model atmospheres thus seems validated for this thesis work.

Chapter 3

Method

This Chapter presents the methods and observations used, and the steps undertaken to achieve the results. Section 3.1 emphasises the importance of evaluating blends to obtain a clean Fe-linelist, and discusses the steps in the procedure undertaken to achieve this. Section 3.2 discusses how an inverted spectrum analysis is performed to obtain astrophysical gf-values, an atomic quantity required to obtain the stellar parameters. Section 3.3 presents a data analysis of the retrieved oscillator strengths. Section 3.4 discusses the retrieval of stellar parameters based on the constructed linelists. Figure 3.1 is a flowchart depicting the major steps of the procedure in the order of completion, and should be used as a complement to the steps discussed in the text. Abbreviations are explained in the relevant Sections.

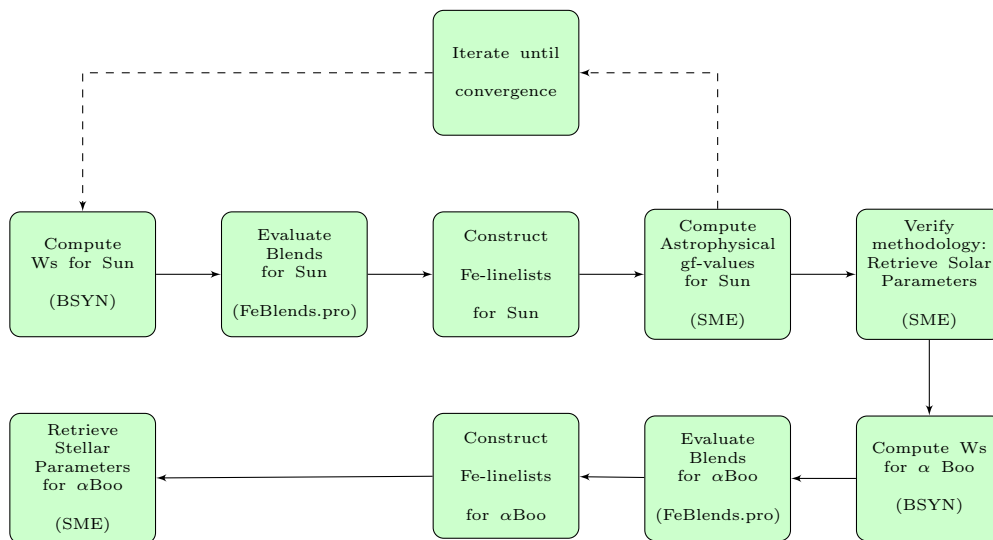


Figure 3.1: A flow-chart depicting the major steps in the procedure. The figure should be interpreted following the arrows that connect two consecutive steps, starting from top left. Parenthesised abbreviations denote the scripts constructed and software packages used.

3.1 Evaluating Blends

To recapitulate from Chapter 2; the methodology relies on spectrum synthesis using the excitation balance of iron lines. These iron lines must cover a large span in (i) *excitation potential* to retrieve T_{eff} , (ii) *equivalent width* to determine ξ_{mic} , and preferably (iii) includes Fe I and Fe II lines to determine $\log(g)$, with metallicities extracted in the process. The synthetic spectrum optimises the fit to each of the selected iron lines by varying the stellar parameters θ_{\star} , effectively updating the line-strengths and line-profiles. The χ^2 -minimised value gives the best set of stellar parameters.

The accuracy and precision of the retrieved θ_{\star} are directly governed by the *completeness* and the *correctness* of the atomic - and molecular line data. If the line data are not *complete*, opacities will be missing and can cause wrong continuum normalisation and missing line-opacities. Spectral synthesis will respond by over/under-estimating θ_{free} in order to minimise the difference caused by missing data. Incompleteness may also result in erroneous line-identification, which can act to produce a larger spread in the evaluated θ_{free} . Even if the line-list is *complete*, the accuracy and precision of the atomic parameters may suffer from systematics and uncertainties caused by compilations of sources, methodology and/or model differences as well as technological limitations. This causes the *correctness* to further propagate into the end result. If a line opacity is over-estimated, the fitting procedure will minimise the synthetic-to-observation difference by changing the θ_{free} that has an effect on the *line-strength* (T_{eff} and/or $[\text{Fe}/\text{H}]$). The situation is further complicated by uncertain opacities belong to blending features, and/or by unknown blends not included in the line data.

Without a method to quantify and minimise the influence of uncertainties associated with the completeness and correctness of the line list, the retrieved stellar parameters will not map the excitation-ionisation balance as implicitly assumed by SME. To quantify the impact of such factors, the methodology must strive to use carefully selected iron lines with minimal blend and good atomic data, compiled into an iron-linelist (Fe-linelist).

Blends must be considered because a spectrum is at every wavelength, λ , the outcome of the total opacity; a composition of the elemental line- and continuum opacities. At a given central wavelength for a transition, all the opacities in the local vicinity of that wavelength contribute to the line formation. To evaluate the impact of blending features, the atomic line data must be assumed. Being uncertain and scarce in the NIR, these are updated against the Sun (refer to Section 3.2) before applying them and evaluating the blends of lines in Arcturus. To this end, synthetic equivalent widths are calculated against a solar-atmosphere with known solar parameters using EQWIDTH. Synthetic equivalent widths are preferred over measured values because this project is *exploring* the NIR for good spectral lines. Measured equivalent widths based on an empirical solar spectrum would implicitly (and carelessly) assume unresolved blends to insignificantly contribute to the total strength of the line, and that the iron line in question had well-determined

reliable atomic data. However, neither of these assumptions can be taken for granted in the exploration of the NIR spectral region.

An IDL script (from hereon referred to by its name; FeBlends.pro) is constructed to read an input in the form of EQWIDTH computed equivalent widths; evaluate the strength and blend of each Fe-line; and based on the evaluation, output an Fe-linelist with associated line-masks for spectrum synthesis to act on. The evaluation is in itself based on selection criteria with threshold values that can be changed manually. Wavelength-normalised *Regions of Interest* (ROI) around the Fe-lines are constructed to account for the natural tendency of spectral lines to broaden with longer wavelengths, within which contributions from atomic- and molecular blends to the observed absorption feature is accounted for. Astrophysical gf-values (the base 10 logarithm of the product of the lower level degeneracy with the absorption oscillator strength¹) are iteratively solved for outputted lines. The updated gf-values alter the line opacities and thus the equivalent width calculations. Therefore, new equivalent widths based on the output gf-values are evaluated and ROIs iteratively updated till convergence. Convergence was normally achieved within one or two iterations.

Constraints on line strength are implemented based on curve-of-growth considerations, restricting the analysis to the use of sufficiently weak lines i.e. unsaturated lines. The equivalent widths of weak lines are proportional to the elemental abundance. A lower bound reduces the influence of noise and unknown blends, since the relative influence of these is inversely proportional to the line strength. This can cause uncertainties associated with continuum placement and the evaluation of the χ^2 -fit. Based on a visual inspection of the noise level in the solar and Arcturus spectra, a lower bound of the line strength measured as an equivalent width of $5 \text{ m}\text{\AA}$ is set. An upper bound of $150 \text{ m}\text{\AA}$ is implemented to reduce the impact of saturation effects (which become prominent as the line approaches the optically thick limit) whilst maintaining sensitivity to the elemental abundance.²

The blend evaluation of lines in the output Fe line-list is implemented by constructing a ROI for each line. This was done by identifying a clean, well-known iron line in the Solar Atlas (Livingston & Wallace 1991). A wavelength position on either side of the line was selected, and acted to mask the region within which blends (hypothetically) could contribute significantly to the observed spectral feature and were to be evaluated. The Doppler formula states that

$$\frac{\Delta\lambda}{\lambda_0} = \frac{\Delta\nu}{\nu_0} = \frac{v}{c}, \quad (3.1)$$

where $\Delta\lambda = \lambda - \lambda_0$ is the wavelength difference of a spectral line of wavelength λ_0 caused by the relative radial motion of the emitter and observer, v , ν denotes the frequency, and

¹Where an oscillator strength is a measure of the intrinsic strength or transition probability of a line.

²According to (Böhm-Vitense 1989, p.129), all lines with an equivalent width $W_\lambda > 15 \text{ m}\text{\AA}$ are not strictly optically thin.

c is the speed of light. $\Delta\lambda$ can be envisaged as a *spread* or *broadening* rather than a wavelength-offset. By considering the ROI as a *spread*, Equation 3.1 can be manipulated to express the ROI in terms of a characteristic doppler velocity, v_{ROI} , which based on visual inspection of the lines was assigned a value $v_{\text{ROI}} = 20 \text{ km s}^{-1}$. This characteristic velocity is used to construct wavelength-normalised ROI for each Fe line i , with boundary wavelengths determined as

$$\text{ROI}_i = \lambda_i \left(1 \pm \frac{1}{2} \frac{v_{\text{ROI}}}{c} \right), \quad (3.2)$$

where λ_i denotes the wavelength of iron line i ; subtraction yields the lower ROI boundary, and addition yields the upper ROI boundary. Figure 3.2 gives an overview of the construction of an Fe-line's ROI, depicting an arbitrarily normalised segment, with flux as a function of some wavelength scale. Absorption-lines are represented with Gaussian profiles, with their summed contributions to the spectral feature as depicted in green. A ROI is centred on the Fe line (black), with limits as indicated by dotted lines. 'Blends' (blue) and 'Outliers' (red) respectively, are incorporated or excluded from ROI based on their central wavelength λ_{central} . If λ_{central} is located within the ROI, its equivalent width is considered in the Fe-blend evaluation; else, it is not. An Outlier can contribute significantly to the the resulting Fe-feature through broad-wing-blending, becoming increasingly important for *strong lines* (with pressure sensitive Lorentzian wings) and *light elements* (low-mass ions have larger velocity dispersions causing stronger Doppler-broadening) lines. This is exemplified by the Outlier wing, invasive with respect to the ROI. The apparent influence of the Outlier on the Fe-feature can be accounted for by correctly mapping the Outlier in spectrum synthesis. This may require the Outlier's gf-value to be retrieved in order for a good fit, but does not influence the blend-evaluation of the Fe-line.

For a ROI, the fractional blend is evaluated. A percentage threshold on the fractional blend in each spectral feature is manually specified, above which it is deemed *clean*. This is implemented by calculating the fractional strength of the feature that the iron line is responsible for (Θ) based on the BYSN equivalent widths;

$$\Theta_i = \left(\frac{1}{W_i + \sum_{j \neq i} W_j(\lambda) + \sum_k W_k(\lambda)} \right) \Bigg|_{\lambda_{\text{central}} \in \text{ROI}_i} \cdot W_i, \quad (3.3)$$

where the indicies i, j, k, λ denote "Fe line i ", "atoms other than Fe", "molecules" and "wavelengths" respectively, and the summations are evaluated across the Fe-line's ROI. Only lines with equivalent widths $5 \text{ m}\text{\AA} \leq W \leq 150 \text{ m}\text{\AA}$ are included. The threshold values on Θ_i is set to 70%, 80% and 95% which will act as references to the Fe-linelist used in later chapters.

Any contribution to a ROI-blend caused by iron lines other than i was omitted based on two arguments. Firstly, the vast amount of iron lines present in the spectra make it

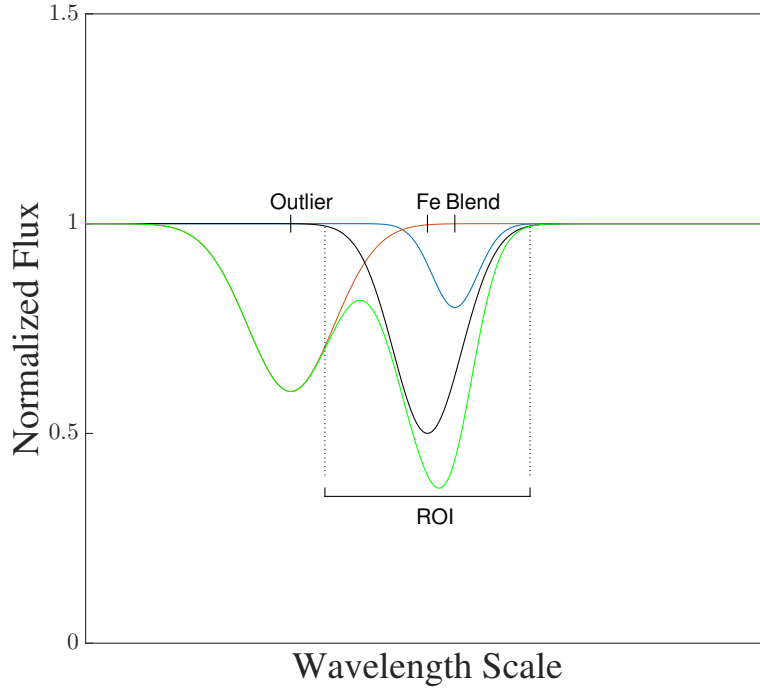


Figure 3.2: Schematic overview of a constructed Region of Interest (ROI). The green curve represents the composite spectral feature as it would appear in a spectral analysis. It consists of the Fe-line of interest (black), an unresolved blend (blue) and an outlier (red) whose strong wing influences the total ROI equivalent width.

probable that lines of interest are blended by iron. Disregarding Fe-blends increased the lines that passed the blend-evaluation by about 35%. Secondly, even if a blend is caused by iron, the assumption of LTE maintains the relative strength of the iron-blend to line i for a given set of stellar parameters. The problems emerge if χ_{exc} of the Fe-blend and the Fe-line are very different, because then a different set of θ_* alters the relative distribution of level-populations (which dependent on χ_{exc}). For fixed gf-values, this alters the relative line-strengths. To avoid such issues, χ_{exc} of lines with Fe blends are examined manually on a line-by-line basis. For most of the Fe-lines with Fe-blends, the excitation potentials of these lines lay energetically close.

It should be noted that since unknown blends may always be present in a spectral feature, the evaluation gives a *minimum* value on the blend-percentage; translating into an "upper bound" on the gf-value (or abundance). The situation is problematised by the implicit assumption that it is the gf-value of the Fe line in the spectral feature that is to be solved for. However, *known* blends in the line core can not be resolved, and can cause a degeneracy with the Fe-line. For this reason, Fe lines with strong (known) core-blends close to

the line-centre were disregarded from the analysis.

The effective temperature of the Sun prevents significant formation of molecules, making molecular blends negligible. In Arcturus, the effective temperature is cool enough for molecules to form. Arcturus’ molecular chemistry is characterised mainly by its Carbon and Oxygen abundances, its structure and its evolutionary stage through dredge-up of C and N cycled/processed material to the photospheric line-forming layers. The most prominent molecular species observed in the NIR spectral bands are specified in Table 3.1.

Table 3.1: α -Boo Molecular Species

Band	Species
J	CN, (C ₂), FeH, OH
H	CN, CO, (C ₂), OH, FeH
K	CN, CO, (C ₂), OH, CH

The molecular line-lists of these vary in quality, with the C₂ line-list (Querci et al. 1971) showing the worst agreement with observations, with lines that tend to be too strong. For this reason, it was disregarded in the synthesis. The molecular line-lists added in the calculation of the total opacities for the Arcturus structure are CN (Jorgensen & Larsson 1990), FeH (as used in the MARCS code, originally from Plez in unpublished work), OH (Goldman et al. 1998), CH (Jorgensen et al. 1996) and CO (Goorvitch 1994) which all show decent agreement in wavelength and strengths.

The above discussed selection criteria regarding line-strength and blends act as a first “sorting”, filtering out lines of interest. In this first stage, further constraints could have been imposed concerning the origin of atomic reference data, and concerning the excitation potential to account for the relative strength variations with θ_* and for the 3D-NLTE effects which may present themselves at low excitation potentials (refer to Section 2.2-2.3). The underlying problem is the tradeoff between *quantity* and *quality* of blend-evaluated lines. Whilst higher-quality lines are desirable, they must be numerous so as to provide leverage for the excitation-balance. Attempting to avoid such dilemmas, further criteria were only considered at a later stage of the procedure, once a working line-list successfully retrieved θ_* .

3.2 Astrophysical gf-values

FeBlends.pro produces an output structure in the form of an Fe-linelist based on the selection criteria and threshold values together with line-masks defined by a lower- and upper wavelength. The line-masks are initially equated to the ROI of each Fe line to define the regions for which θ_{free} will be minimised on. The presence of spectral artefacts caused by bad and/or hot pixels, and bad spectral normalisation against the telluric atmosphere motivates the masks to be updated on a line-by-line basis upon visual inspection. This inspection of the synthetic fit to the solar spectrum further revealed an evident lack of accurate atomic data, as exemplified in Figure 3.3.

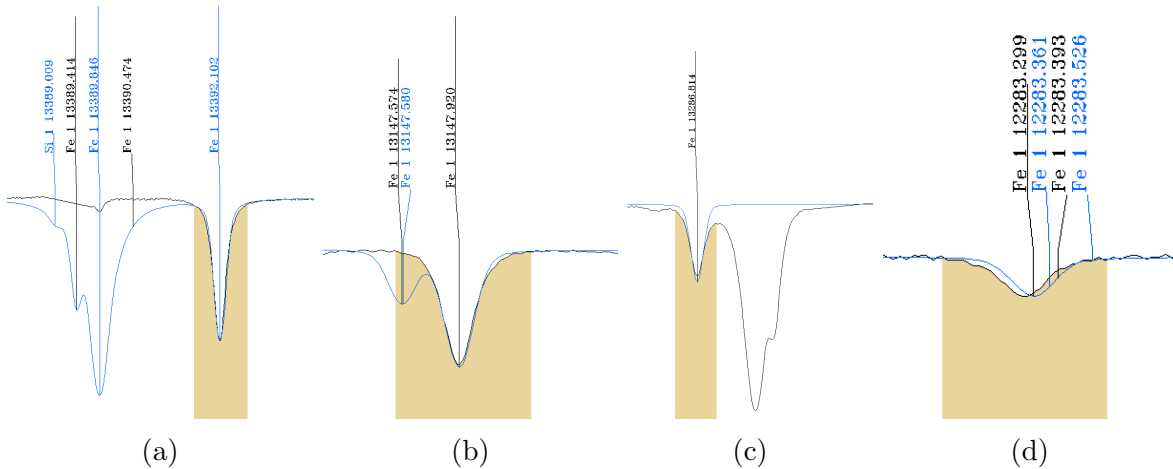


Figure 3.3: Synthetic spectra (blue) do not reproduce observed spectra (black), resulting from incorrect atomic data. Yellow regions represent line-masks. In (a) and (b) this is caused by errors and uncertainties in the gf-values of known transitions or gf-values assigned to wrongly identified transitions. In (c) the absence of atomic data prevents the observed spectral feature from being reproduced. In (d) a correct gf-value has been assigned to the wrong transition, or the energy levels associated with the line have not converged in atomic structure calculations.

The VALD database (Piskunov et al. 1995; Heiter et al. 2008) is a collection of critically evaluated atomic parameters based on laboratory, computational and extrapolated values. The ambition is to use well-determined atomic data. For simple systems, this can be obtained from atomic structure calculations. However, for complex systems like neutral and singly ionised Fe, these must be measured experimentally. Apart from wavelengths and excitation potentials, accurate oscillator strengths are the most critical parameters required as input for spectral synthesis and for reliable chemical abundances in stellar atmospheres. The problem is that the NIR spectral region has been overlooked in favour of other spectral regions in the past, and therefore remains relatively unexplored. Further, oscillator strengths of complex atoms like Fe are hard to determine experimentally because it is hard to populate the levels that give rise to NIR transitions and the procedure requires measurements of the *radiative lifetime* and of all the *branching fractions* from the same

upper level (measured in emission). Depending on the states and atomic selection rules, these transitions can lie in different wavelength regions; each wavelength region requiring its own detector. The different spectra must then be normalised to the same intensity scale.

To overcome the missing atomic data, astrophysical gf-values are solved using an inverted analysis of the output Fe-lines against solar spectra, extracted from Livingston & Wallace (1991). To determine astrophysical gf-values against the Sun, the solar parameters (θ_{\odot}) have to be specified, taken to be $T_{\text{eff}\odot} = 5777\text{K}$, $[\text{Fe}/\text{H}]_{\odot} = 0$ dex (by definition), $\log(g)_{\odot} = 4.44$ dex, $v_{\text{mic}} = 1.0 \text{ km s}^{-1}$. To refine the pre-normalised spectrum, SME allows the user to specify continuum masks for a *global* continuum placement, or *locally* by a linear fit in each specified segment. The synthetic fit to a line was observed to be quite sensitive to the continuum placement. Accordingly, carefully placed local masks and segments were constructed on a line-by-line basis, by specifying continuum regions on either side of the investigated line-profile. This worked well, and was observed to give robust measurements.

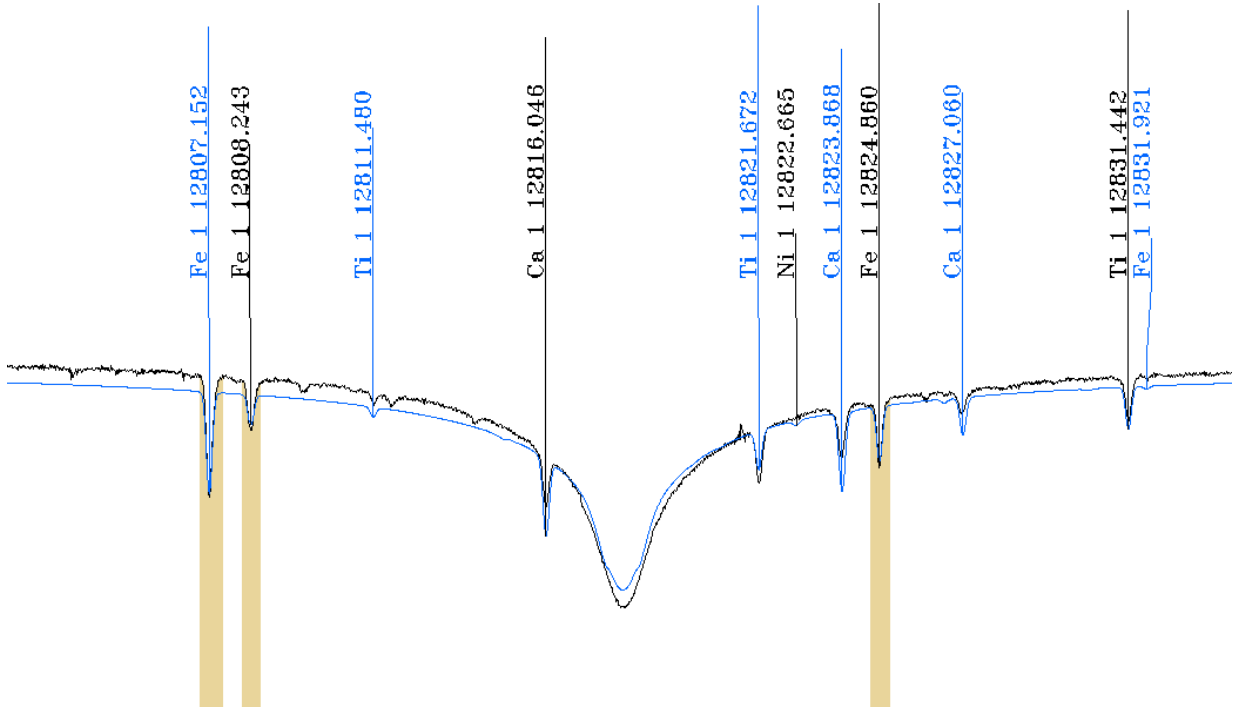


Figure 3.4: A strong hydrogen transition with broad Lorentzian wings exerting influence on the local continuum placement of other lines in its vicinity. The synthetic spectrum is depicted in blue, the observed spectrum in black. Yellow regions represent line-masks. This can cause the gf-value (or equivalently the abundance) of iron, as determined based on the Fe I transitions $\lambda 12807.152\text{\AA}$ and $\lambda 12808.243\text{\AA}$ to be seriously off, if not dealt with on a line-by-line basis. To minimise the resulting effect on the stellar parameters, such problematic transitions were avoided in the analysis.

The regions were selected by considering noise, presence of line opacities, and were placed to avoid broad Lorentzian wings of strong Hydrogen lines. To show the extent to which

such Hydrogen wings may influence the local surrounding (especially in terms of the continuum), Figure 3.4 shows a representative Hydrogen feature. This significantly reduced the uncertainty that a globally well-chosen continuum could have on individual lines.

In the weak line approximation, the equivalent width W of a line is,³

$$\log\left(\frac{W}{\lambda}\right) = \log(C) + \log(A) + \log(gf\lambda) - \theta_{\text{exc}}\chi_{\text{exc}} - \log(\kappa_{\nu}), \quad (3.4)$$

where C is a constant for a given star and for a given ion, A represents the number abundance for the element relative to Hydrogen, gf denotes the gf -value, $\theta_{\text{exc}} = 5040/T_{\text{exc}}$ is a factor containing the temperature and appears by expressing the partition function as a power of 10 rather than the natural logarithm, κ_{ν} is the continuum opacity, and the division by wavelength λ normalises Doppler-dependent phenomena. For a line without a measure of the oscillator strength, Eq. 3.4 states that the observed W is degenerate in A and gf -value.

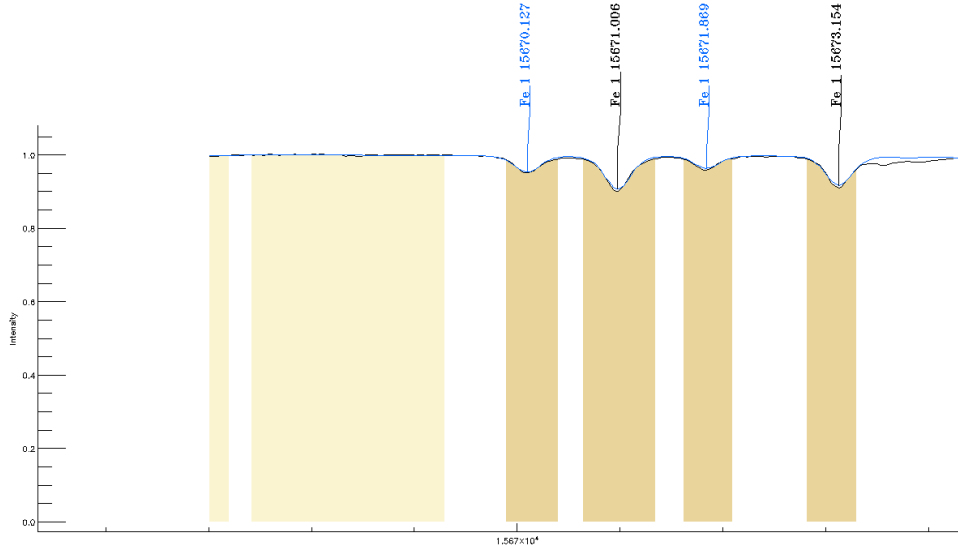


Figure 3.5: Optimised gf -values, solved using an inverted analysis of solar H-band observations. The synthetic spectrum is depicted in blue, the observed spectrum in black. The faint- and dark yellow regions represent continuum- and line-masks. For the sake of clarity, a spectral segment with low noise and an absence of telluric lines and molecular features is used.

Assuming a well-known solar iron abundance of $A(\text{Fe})_{\odot} = 7.50$ (Asplund et al. 2009), the synthetic fit to the empirical spectrum is minimised by setting the gf -value as a free parameter. The updated gf -value is used as a fixed input, and v_{mac} is set free. This is important

³The result is achieved by expressing the equivalent width in terms of the frequency-dependent line- and continuum opacities, and integrating across the line-profile. For a complete derivation, see (Gray 2008, p.388 - 389)

because the χ^2 -minimisation is sensitive to the line profile, and hence the macroturbulence broadening can effect the evaluated fit. The astrophysically determined gf-value is the value retrieved upon convergence of v_{mac} and the gf-value, and minimises the synthetic fit of a specified line. Examples of optimised fits are shown in Figure 3.5. The (updated) value replaces the VALD-assigned gf-value in the input atomic line data.

The problem with this procedure is that possible 3D- and NLTE effects, unknown blends, uncertainties in the model atmosphere and the input model parameters are 'truncated' in the astrophysical gf-value. This means that although useful for a differential analysis, where systematic model errors should cancel out, they are problematic for stars whose parameters diverge from the benchmark star, which in this case is the Sun.

3.3 Data Analysis

Transitions, reference- and astrophysical gf-values are tabulated (Table A.1), with lines grouped according to excitation potential χ_{exc} , and internally by wavelength (λ_{band}) where the subscript refers to the atmospheric band (J or H) it belongs to. For each transition, the VALD gf-value (and reference therein), the determined astrophysical gf-value and the difference; $\Delta \log(\text{gf}) = \log(\text{gf})_{\text{VALD}} - \log(\text{gf})_{\text{astroph}}$ is given. An attempt is made to see whether lines from specific χ_{exc} show better or worse agreement with VALD values by noting the standard deviation (σ) in the $\Delta \log(\text{gf})$ respectively. The difference in initial input and final gf-values span across a width reaching from -2.7 dex to 2.5 dex, i.e. factors of up to 500 in the obtained abundance, depending on the Fe-line and source of the gf-value used in the analysis. This discrepancy motivates a study to see whether the required updates suggest a random line-to-line scatter, or whether systematic trends in the cited values are present.

Figure 3.6 shows a partial Fe I energy-level diagram depicting χ_{exc} of the observed J- and H- band transitions grouped according to configuration and parent term. The dashed horizontal line at 7.9 eV indicates the ionisation energy of Fe I. Boxes trace the energy interval for all levels of a given nl -symmetry. The dotted lines connect boxes of the same nl -symmetry belonging to different parent-terms for a given configuration. An arbitrary "cut" in $\Delta \log(\text{gf}) = 0.097$ dex ($\pm 25\%$ in abundance) was made to see if we could learn something about transition-strength accuracies in general, and whether or not these follow trends with atomic structure. Energy levels drawn in black refer to excitation potentials with at least one transition below the cutoff difference, whilst red ones refer to levels where all transitions fell above the cut.

Figure 3.6 suggests that the difference in gf-value is uncorrelated with the atomic structure. If this difference is interpreted as a "quality" test, this means that Fe-lines for an analysis and determination of θ_* cannot be selected based on atomic structure/the terms and configuration that a set of transitions belong to. With this in mind, it is interesting

to note that most of the transitions seem to originate from levels in the $3d^6(^5D)4snl$ configuration; an effect probably apparent because it includes the lowest lying 4p-levels. A peculiar set of levels are those grouped together in the $3d^7(^4F)5s$ term. These all show the presence of at least one transition which has an astrophysical gf-value determined in this thesis that stands in good agreement with the VALD-assigned value. Although these levels were suspected of hiding transitions with experimental measurements, a closer inspection revealed that this was not the case. Rather, the levels gave rise to a lot of transitions making it probable to identify a transition in agreement.

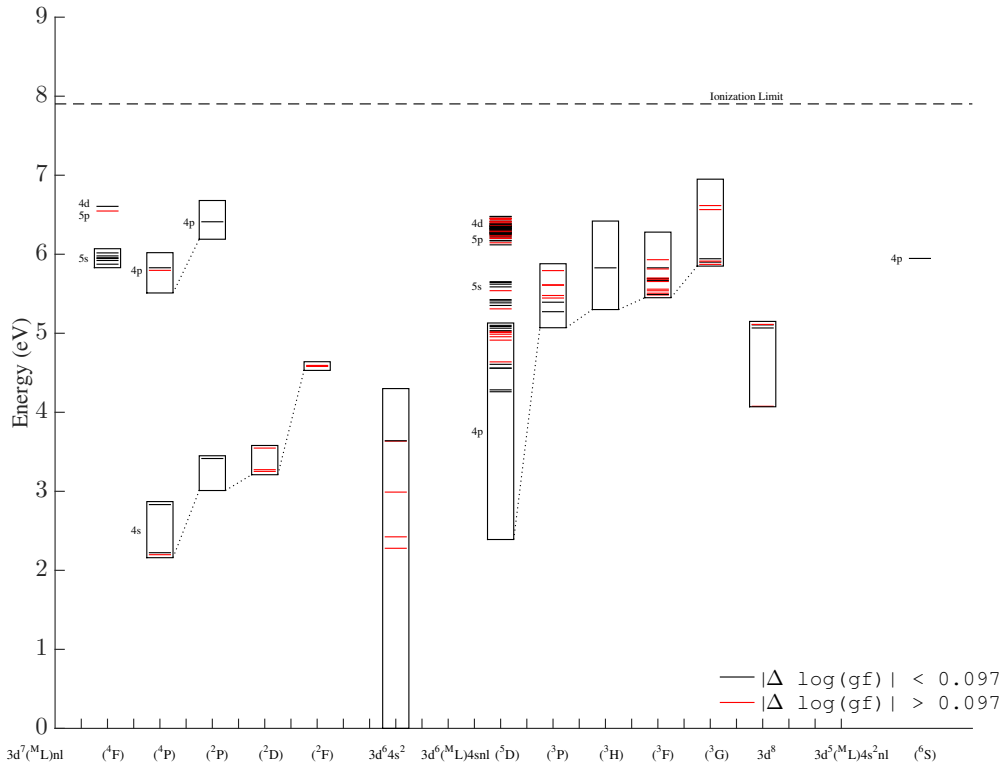


Figure 3.6: Partial Fe I energy-level diagram in terms of χ_{exc} , grouped according to configuration and parent term (based on the J- and H-band solar spectra). Black lines indicate levels with at least one transition whose assigned literature gf-value is in agreement with that of this work, whilst red lines indicate levels without gf-values in agreement. The discriminator is chosen to be at a gf-value giving a difference of $\pm 25\%$ yield in abundance. The dashed horizontal line at 7.9 eV indicates the ionisation energy of Fe I. Boxes trace the energy interval for all levels of a given nl -symmetry. The dotted lines connect boxes of the same nl -symmetry belonging to different parent-terms for a given configuration.

To quantify the differences in oscillator strengths and unveil any underlying trends, the origin of each literature value for the Fe-lines as referenced by the VALD database was studied. Table 3.2 shows the number-count (N) of transitions with gf-values determined by a reference, together with the number-count *mean* and *standard deviation*. In the following analysis, references with $N \leq 5$ are disregarded on the grounds of poor statistic potential.

The values obtained by O’Brian et al. (1991) show *less* scatter than other sources, demonstrated by the significantly lower mean and standard deviation. Upon closer inspection, the O’Brian et al. (1991) values turned out to be the only source determining oscillator strengths *experimentally* using lifetimes and branching fractions rather than a *computational* approach. This testifies to the difficulties of theoretically calculating gf-values for complex systems such as Fe I (Cowan 1981).

Table 3.2: Literature Values Statistically Compared

Reference	N	$\langle \Delta \log(gf) \rangle$	σ	Method
(Kurucz 2007)	397	0.01	0.50	Theor. Calc.
(Kurucz 2006)	2	0.21	0.03	Theor. Calc.
(Kurucz 1988)	1	0.56	-	Theor. Calc.
(Biemont et al. 1999)	1	0.43	-	Theor. Calc.
(Raassen & Uylings 1998)	5	0.21	0.27	Theor. Calc.
(Kurucz & Peytremann 1975)	13	0.32	0.80	Theor. Calc.
(O’Brian et al. 1991)	10	0.14	0.18	Experimental
No Ref.	29	0.12	0.42	-

The difficulty arises because calculations must account for the mutual electrostatic repulsion of the electrons. For a many-electron system, this interaction can no longer be treated as a perturbation but requires accurate computation of the radial wave functions. These are difficult to determine since all possible atomic states must be accounted for, and so complicates the determination of oscillator strengths. Further, complex spectra have a lot of levels which increases the probability for level-mixing.

Despite of a large *spread* ($\sigma = 0.5$ dex), the Kurucz (2007) comparison reveals a remarkably low *mean* ($\langle \Delta \log(gf)_{K07} \rangle = 0.01$ dex). In light of the uncertainties associated with computed oscillator strengths this requires an explanation. From a *practical* point of view, Kurucz atomic structure calculations were motivated by a need of extensive atomic data, required for calculations of opacities in stellar envelopes and Rosseland mean opacities (Seaton et al. 1994). Since the science was interested in total opacities and mean values, the exact contribution and values assigned to individual lines were not studied in detail. From a *fundamental* perspective, atomic structure calculations make use of ‘oscillator strength sum rules’ (Cowan 1981). These allow the sum of all oscillator strengths from a level (valid for lower as well as upper levels) to be determined, even if the relative

strengths of the individual transitions are complicated by configuration-interactions and level-mixing. If many of the observed transitions share common states, this would explain how although individual oscillator strengths show large scatter, the use of the sum rules have maintained the correct total, giving a low mean difference.

It is interesting to note that a significant number of lines are grouped according to the label “No Reference” and show an offset mean. These lines have likely been assigned a gf-value without further investigation, because measured energy-levels and atomic transition rules suggest lines to be there. Ironically, the scatter of these lines is comparable to those of calculation-based values.

As we intend to use a subset of the lines for which we have solved gf-values to determine stellar parameters, the quality of individual lines is paramount. Inevitably, a decision must be made as to what sources to trust. On the level of individual lines the sum-rules do not hold, leaving computational values misleading. Sticking to the use of only astrophysical gf-values makes the set of Fe-lines homogenous, however restricts the Fe-linelist use to stars of similar parameters as the benchmark star for which gf-values were solved. Another option to be considered is to restrict the analysis to the use of the O’Brian et al. (1991) experimental measurements. This would also provide uncertainties - an advantage compared to calculated values; the greatest concern being the leverage that only 10 lines (ideally) have on constraining T_{eff} .

Recent emphasis on the NIR has motivated further laboratory measurements of gf-values. Going beyond the VALD database, Ruffoni et al. (2013) and Ruffoni et al. (2014) expanded the library of lab-measured Fe I oscillator strengths in the NIR significantly.⁴ To investigate the general agreement, Figure 3.7 shows a comparison between the blend-evaluated astrophysical gf-values determined in this thesis and the experimental values as obtained by O’Brian et al. (1991) and Ruffoni et al. (2013). The dotted black line shows a hypothetical one-to-one correspondence whilst the blue line shows a straight line fitted through the data.

The astrophysical gf-values stand in good agreement with experimental values, indicating that carefully selected lines, blend-evaluated and with carefully chosen continuum points and line-masks and known θ_* can reproduce the correct values. In fact, the only reason for a departure from the one-to-one correlation is the two outliers with respect to Ruffonis measurements, which force the linear fit towards a shallower slope. Initially, this discrepancy was thought to be caused by uncertainties in the experimental values. However, with typical uncertainties of 0.09 dex, these values are too well determined to explain the observed difference.

⁴In fact, Ruffonis measurements made use of radiative lifetimes *calculated* from Kurucz (2007) and are therefore “pseudo-experimental”.

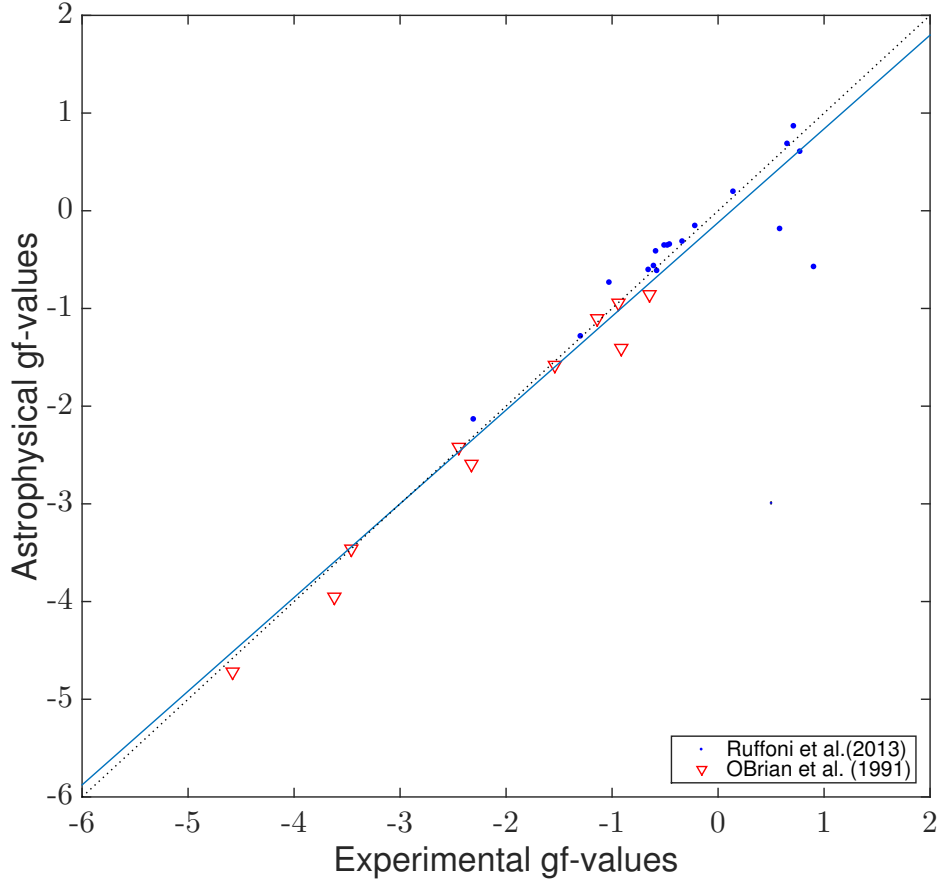


Figure 3.7: Comparison between astrophysical (this work) oscillator strengths (gf-values) and experimental gf-values where such exist. Blue dots represent values determined by Ruffoni et al. (2013), whilst red triangles represent values measured by O’Brian et al. (1991). The black dotted line represents a theoretical one-to-one correspondance. The blue line is a linear fit through the data points. Typical experimental uncertainties are of the order 0.09 dex, too small to be depicted meaningfully.

Alternatively, the lines associated with these gf-values were thought to be strong, reaching towards the upper limit on the threshold value imposed on line-strength ($\sim 150 m\text{\AA}$). If so, they could have been sensitive to the adopted ξ_{mic} , or have line-cores which form in the outermost photospheric layers where they would have encountered NLTE effects which made the determination of astrophysical gf-values problematic. However, the two lines $\lambda 15591.500 \text{ \AA}$ and $\lambda 15294.904 \text{ \AA}$ have equivalent widths of $30 m\text{\AA}$ and $65 m\text{\AA}$ respectively, making them insensitive to such effects. Upon closer inspection, $\lambda 15294.904 \text{ \AA}$ has been fitted to a resolved feature/bump in the wing of an other Fe line in an attempt to use them both. In the χ^2 -minimisation there is a degeneracy as to which one of them to vary to retrieve the correct value, and this explains the observed error in the astrophysical value. A similar "explanation" results in the obtained value for $\lambda 15591.500 \text{ \AA}$. It turns out that

it is blended by another Fe-line with an equivalent width of $267 \text{ m}\text{\AA}$. However, being only 0.07 \AA apart in central wavelength, the one was mistaken for the other in the solution for astrophysical gf-values. Since the blending Fe line is so strong, the whole feature should have been omitted. Yet, it does lead to an interesting comment regarding the change in relative strengths of Fe-lines with different excitation potentials and at different temperatures.

An astrophysically determined gf-value wrongly assigned to one out of two Fe-lines in an unresolved spectral feature can still be useful, provided (i) it reproduces the observed spectral feature, and (ii) that, under the assumption of LTE, the difference in excitation potentials $\Delta\chi_{\text{exc}}$ of the two lines is small as compared with the product of the Boltzmann constant with the temperature $k_B T$. For the two lines in question, namely the $\lambda 15591.500 \text{ \AA}$ and its blending companion $\lambda 15591.493 \text{ \AA}$, the difference is $\Delta\chi_{\text{exc}} = 6.35 - 6.24 = 0.11 \text{ eV}$. Making use of the Boltzmann factor, the Sun at $T = 5777 \text{ K}$ gives a level population ratio of ~ 0.8 , whilst Arcturus at $T = 4286 \text{ K}$ gives a corresponding ratio of 0.74 . This means that the change in relative line-strengths of the lines caused by the difference in level-populations for the two temperatures are of the order 6% , which corresponds to a factor $\log(1.06) = 0.025 \text{ dex}$. This change is low and on the order of the uncertainty in the astrophysical gf-values (refer to Section 4.4 for uncertainties). If it was not for the large equivalent width ($267 \text{ m}\text{\AA}$) of the blend exceeding the threshold value, the above argument would justify the inclusion of the line in the hypothetical line-list. As a word of caution however, it should be noted that this difference of 0.025 dex is a systematic effect in the line, which in principle could (and should) be avoided by disregarding the line at this stage.

Following Niemczura et al. (2014) and Piskunov et al. (1995), the LTE central line opacity (l_{λ_c}) can be expressed as

$$l_{\lambda_c} \propto gf\lambda_c^2 e^{-\chi_{\text{exc}}/k_B T}, \quad (3.5)$$

and can be used as a proxy for the equivalent width through the relation $\log(W_\lambda) \propto \log(l_\lambda/\kappa_\lambda)$ and a slowly varying κ_λ across the line-profile.

To investigate how $\Delta \log(\text{gf})$ correlates with different parameters, Figures 3.8, 3.9, 3.10 and 3.11 show the difference as a function of gf-values, wavelength λ (\AA), excitation potential χ_{exc} and a proxy for equivalent width. The data has been categorised according to reference by colour and symbol; red dots (Kurucz 2007); magenta crosses (Kurucz 2006); black '+' (Kurucz 1988); cyan '*' (Biemont et al. 1999); yellow diamond (Raassen & Uylings 1998); blue circles (no reference); green squares (Kurucz & Peytremann 1975); and black triangles (O'Brian et al. 1991). The dotted horizontal lines denote differences in $\log(\text{gf})$ values of 0.097 dex ($\pm 25\%$).

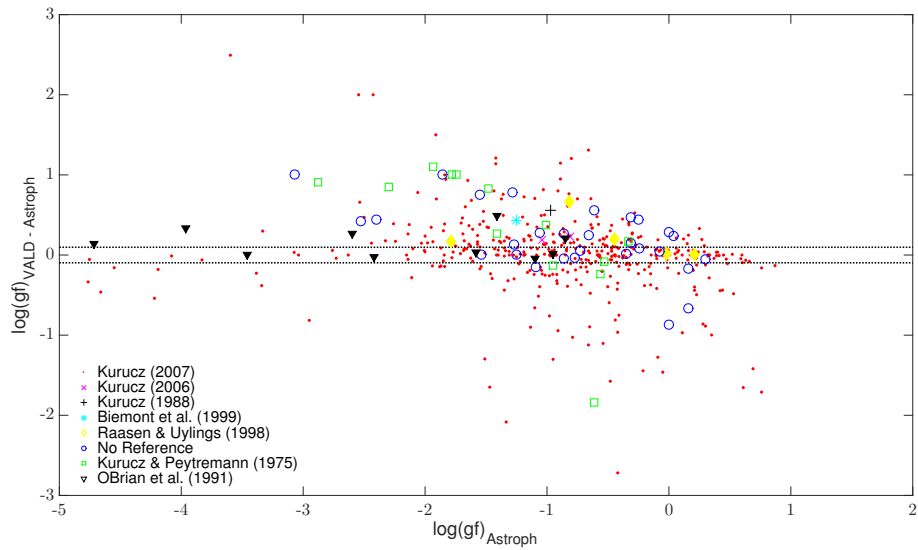


Figure 3.8: Comparison between this work's gf-values and those published in the VALD database, plotted as a function of this work's gf-values. Dotted horizontal lines indicate differences in gf-values corresponding to $\pm 25\%$ yield in abundance. References are (Kurucz 2007); (Kurucz 2006); (Kurucz 1988); (Biemont et al. 1999); (Raassen & Uylings 1998); (no reference); (Kurucz & Peytremann 1975); and (O'Brian et al. 1991). Correspondingly, black triangles are the only data points based on experimental measurements.

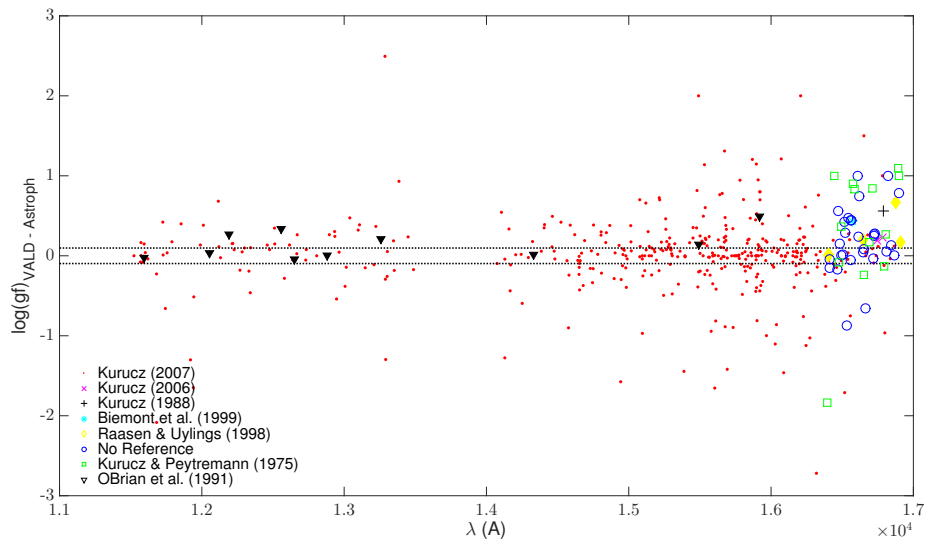


Figure 3.9: A comparison between the gf-values of this work and those published in the VALD database, plotted as a function wavelength λ . References and figure nomenclature are as Figure 3.8.

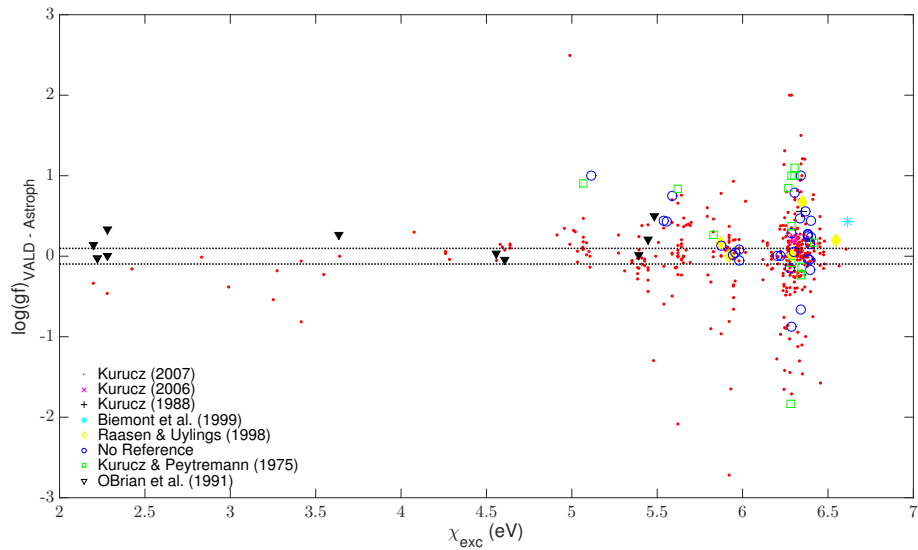


Figure 3.10: A comparison between the gf-values of this work and those published in the VALD database, plotted as a function excitation potential (eV). References and figure nomenclature are as Figure 3.8.

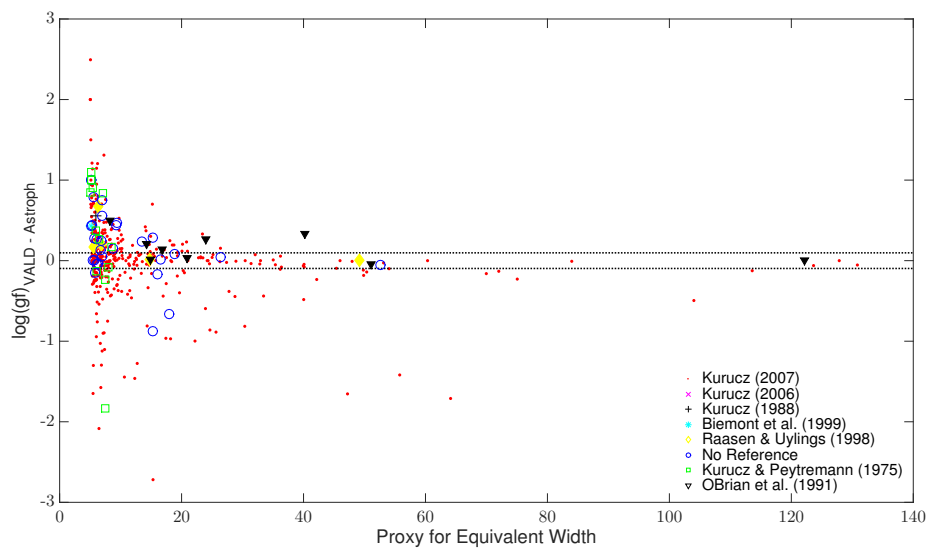


Figure 3.11: A comparison between the gf-values of this work and those published in the VALD database, plotted as a function of the proxy for equivalent width, as given by Eq. 3.5. The data points have been offset horizontally by adding a constant to avoid clumping towards the lower equivalent width limit. References and figure nomenclature are as Figure 3.8.

From Figure 3.8 there seems to be a large scatter in the plotted differences, independently of the gf-value investigated. There is, however, an obvious trend with method - namely that the difference calculated with respect to experimentally determined oscillator strengths (black triangles) shows less scatter. This reflects the tabulated data (Table 3.2) and the one-to-one correlation as discussed for Figure 3.7. A negative slope towards increasing gf-values may be suggested. Assuming the gf-value to (on average) trace the line-strength, this could be indicative of a larger fraction of unknown blends in strong lines. However, the absence of the correlation with experimental values speaks against it, and may alternatively suggest that it is an effect caused by the computational methods. No further analysis of this apparent trend was attempted.

Plotted as a function of wavelength (Figure 3.9), the experimental measurements of O’Brian et al. (1991) are concentrated towards shorter wavelengths whilst the theoretical calculations seem to be concentrated towards longer wavelengths, ultimately leading to an increased scatter with wavelength. The same trend is observed for excitation-potential χ_{exc} (Figure 3.10), and is a result of the level-separation decreasing as you move up in the term-diagram. With the level-separation becoming narrower, the significance of level-mixing will increase. Since calculations have trouble dealing with such interactions, the scatter towards high excitation potentials is predicted. In plotting the difference as a function of the proxy for equivalent width (Figure 3.11), most data points fall in the lower end, reflecting the underlying constraints on line-strength, biased towards weak lines. Since smaller equivalent widths are more sensitive to blending features and noise, the increased spread at the lower end could be interpreted as an effect produced by the astrophysically determined value.

3.4 Retrieving Stellar Parameters

With updated gf-values and a macro-turbulence broadening applied to minimise the differences in the χ^2 -fit, line- and continuum masks were visually inspected in SME against a solar spectrum. These were updated so that telluric normalisation artefacts and bad pixels were avoided. For fixed gf-values and a well-determined v_{mac} , θ_* were set globally free in an attempt to retrieve the solar parameters using the Fe-linelist. θ_* involve degeneracies on their effect on the lines, and ideally these degeneracies could be broken by solving for parameters in different steps; yet spectrum synthesis uses a χ^2 -minimisation routine, and therefore a θ_* cannot be solved independently of another. Two procedures (P1 and P2) were undertaken to break the degeneracies. In P1, one parameter was initially set free for the remaining parameters fixed. θ_{free} was updated to the value optimising the fit, and set as fixed. In this way, θ_{free} was stepwise permuted across the set of stellar parameters and repeated until all θ_* converged. In P2, all parameters were set free simultaneously, making the χ^2 -plane multi-dimensional and complex. If the parameters did not converge with literature values assuming the astrophysical gf-values of this project as input, the Fe-linelist was altered. The alterations involved optimising mask sizes and limits, removing questionable fits, and adding lines that could break the degeneracies in the parameters. A

convergence of the retrieved parameters, such that $\theta_{\star} \rightarrow \theta_{\odot}$, indicated that the methodology was viable for the determination of stellar parameters.

Blends were evaluated for an Arcturus structure, with $\theta_{\alpha\text{Boo}}$ taken from Ramírez & Allende Prieto (2011), using a line-data with the updated astrophysical gf-values (as solved against the Sun). It is important to re-evaluate the blends of Fe-lines because the structure and composition of Arcturus differs from the Sun. Apart from the presence of molecules, its structure alters the line and continuum opacities, which can change the relative strengths of lines. Based on the outcome, an initial Fe line-list was constructed.

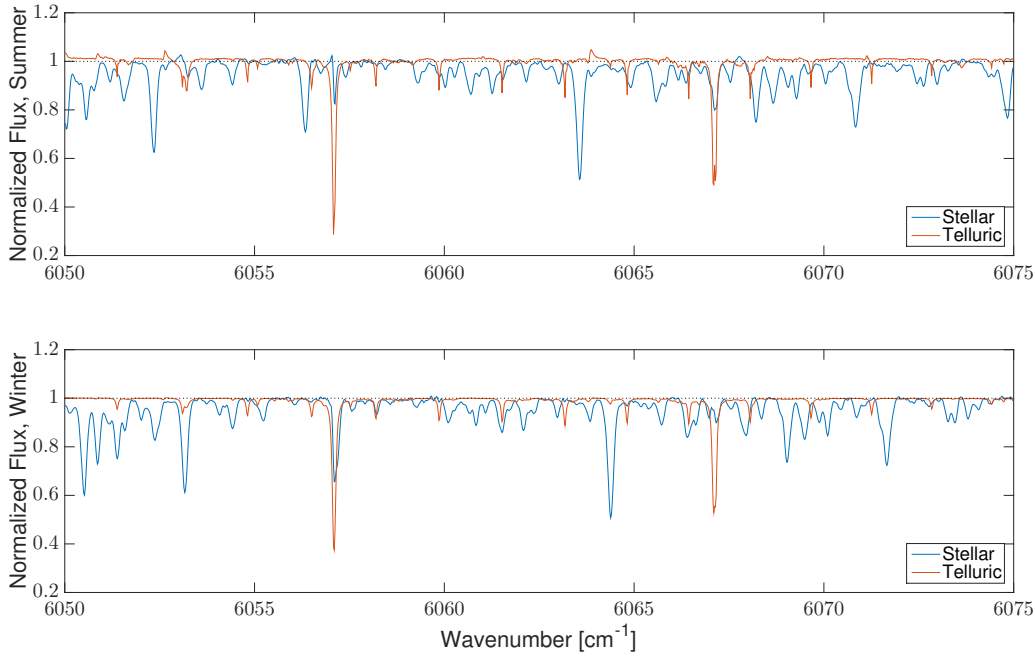


Figure 3.12: Comparison of an Arcturus summer- and winter spectral segment (upper and lower panel respectively), plotted as a function of wavenumber. The segment corresponds to the wavelength-region around $\lambda\lambda$ 1.64- 1.65 μm . The red and blue curves denotes the telluric and stellar spectra respectively, and the dotted line denotes a continuum normalisation to unity. The telluric lines have a fixed position because they arise in the rest-frame of the observer whilst the orbital motion of the Earth causes shifts in the stellar features (red) as observed at different times.

The Arcturus Atlas includes summer and winter spectra. For a given transmission band, these were compared to check the quality of the data. Figure 3.12 shows a flux-normalised summer and winter segment (top and bottom respectively). The reduced stellar spectrum (normalised to a continuum level of unity and divided by the telluric spectrum) is plotted in blue, the telluric spectrum is plotted in red, and the dotted horizontal line in black marks an ideal continuum level at unity. Telluric lines tend to be sharper, an effect caused by a different atmospheric structure. The division by the telluric spectrum introduces a "residual" noise, which increases the noise level and as such, reduces the quality of the

observations.

Preference to winter observations were given for all spectral bands based on the quality of the data. The summer spectra in general show stronger telluric lines (probably caused by increased atmospheric humidity and turbulence), which in turn gives rise to more spectral artefacts and affect the continuum normalisation. Ground-based observations are performed stationary with respect to the telluric atmosphere. However, due to the change in relative motion of Arcturus caused by the orbit of Earth around the Sun between winter and summer, the stellar spectrum is shifted with respect to telluric lines - an effect that is observed in Figure 3.12. This allowed an alternation between the spectra in case a spectral feature in the reduced stellar spectrum was unsatisfactorily reproduced after normalisation or blocked by a telluric feature in the winter spectra.

SME has difficulty to adjust large wavelength offsets. Therefore, a radial velocity shift v_{rad} was manually introduced by identifying absorption features to known features in the Arcturus Atlas. Once a gross value had been applied, v_{rad} was set as a free parameter, and SME refined the fit. For fixed stellar parameters and pre-determined Fe line-list of 70, 80 and 95% cleanness, v_{mac} was solved for. Line- and continuum masks were optimised on a line-to line basis, based on a visual examination of the spectra. For Arcturus, this was a time-consuming task due to the contribution of molecular lines, and special care had to be taken. The stellar parameters of Arcturus were set as free parameters and solved for according to the previous schemes. As a consequence of the absence of Fe II lines in the H-band (as confirmed by Smith et al. (2013)), the surface-gravity was fixed to the literature value throughout the procedure.

Chapter 4

Results

This chapter presents the results of the thesis. Section 4.1 investigates how well the methodology worked in retrieving the solar parameters. Section 4.2 analyses the final linelists, optimised for Arcturus. Section 4.3 investigates θ_* retrieved for Arcturus using the constructed Fe-linelists. Section 4.4 estimates the uncertainties in the determined Teff.

4.1 Retrieval of Solar Parameters

The solar parameters, θ_\odot , were retrieved as a consistency check of the methodology. Since different Fe line-lists are constructed for the J and H bands, θ_\odot are retrieved for each band separately. This also allows a comparison between θ_\odot retrieved for the different bands. I adopt the known literature values as $T_{\text{eff}} = 5777$ K, $\log(g) = 4.44$ dex, and the metallicity, per definition, is set to $[\text{Fe}/\text{H}] = 0.00$ dex. Radial and rotational velocities of $v_{\text{rad}\odot} = 0.52$ km s⁻¹ and $v \sin i = 1.66$ km s⁻¹ were assumed as initial input, based on prior work by Ryde (private communication), and were retrieved for the J-band when set as free parameters in SME. The macroturbulence of the Sun in the J-band had to be updated from an initial value of 1.61 km s⁻¹ to $v_{\text{mac}} = 1.77$ km s⁻¹. A microturbulence of $\xi_{\text{mic}} = 1.0$ km s⁻¹ was determined.

Using updated gf-values and fixing the parameters as specified above, θ_\odot were determined in a set of SME-jobs. When Teff was set free, SME retrieved a temperature $T_{\text{eff}\odot} = 5773$ K. When Teff and $[\text{Fe}/\text{H}]$ were set free simultaneously, a small degeneracy was revealed, with SME minimising the fit for $T_{\text{eff}\odot} = 5767$ K and $[\text{Fe}/\text{H}]_\odot = -0.004$ dex using an Fe-linelist with a 70% threshold on the blends; and $T_{\text{eff}\odot} = 5766$ K and $[\text{Fe}/\text{H}]_\odot = -0.005$ dex using an Fe-linelist with a 95% threshold on the blends. Setting ξ_{mic} free simultaneously revealed no further degeneracies in the retrieved values.

The obtained values for $T_{\text{eff}\odot}$ and $[\text{Fe}/\text{H}]_\odot$ are *mean* values, obtained for a grid of initial parameters, θ_{init} , designed to test the stability of the solution and the ability of SME to retrieve the *global* minimum in the χ^2 -plane. Being the primary concern, T_{init} was the only

θ_{init} varied. This was conducted in steps of 100 K for $4500 \leq T_{\text{init}} \leq 6500$, with additional measurements for $T_{\text{init}} = 5750, 5760, 5770, 5777, 5780, 5790$ K in order to see that SME's minimisation routine is well-behaved around the null-hypothesis $\text{Teff}_{\odot} = 5777$ K. The uncertainties in effective temperature and metallicity that variations in T_{init} propagated to were negligible, amounting to spreads of $\sigma_{T_{\odot}}(T_{\text{init}}) = \pm 4$ K, and $\sigma_{\text{FeH}}(T_{\text{init}}) = \pm 0.003$ dex respectively. The uncertainty induced by the selected starting value on the Sun is therefore disregarded in the remainder of this thesis as its significance is overwhelmed by other uncertainties (refer to Section 4.3 for a qualitative and quantitative discussion regarding the sources of errors and how these propagate into the effective temperature determination).

For the H-band, the macroturbulence and the radial velocities were determined to $v_{\text{mac}} = 3.26 \text{ km s}^{-1}$ and $v_{\text{rad}} = -0.54 \text{ km s}^{-1}$ using a subset of Fe-lines with well determined gf-values. For only Teff set free, the effective temperature was determined to be $\text{Teff} = 5777$ K using a high-quality and visually inspected set of 60 lines, and $\text{Teff} = 5780$ K using a long list (~ 400 Fe lines) where a larger amount of blends (30%) have been allowed. When the metallicity was set free simultaneously with the effective temperature, the obtained values were $\text{Teff}_{\odot} = 5754$ K and $[\text{Fe}/\text{H}] = -0.01$ dex, respectively.

The retrieved parameters, θ_{\odot} , seem to indicate the presence of a degeneracy in effective temperature and metallicity. In theory, these are only degenerate on a line-by-line basis as a change in the line-strength can be achieved by varying either one of these parameters. However, for a *set* of iron-lines, the degeneracy should be broken; a change in $[\text{Fe}/\text{H}]$ affects the strength of all Fe lines in the same way, whilst a change in Teff affects the relative strengths since it alters the whole distribution of level-populations. The presence of this degeneracy stresses how important it is to maintain lines that have low- and high χ_{exc} with well determined gf-values.

4.2 Arcturus-optimised Fe-linelist

Based on the selection criteria, threshold values, blend-evaluation and the visual inspection and masks evaluated on a line-by-line basis, Table 4.1 and Table 4.2 show the adopted Fe-linelist for the J- and H-band respectively. These are sorted according to wavelength, with the associated excitation energy and the recommended gf-value of each transition. Each transition has been assigned a "quality-flag", based on the visual examination of the fit and on the blend-percentage evaluated for the line. Two stars is indicative of the highest level of cleanness. This means that the oscillator strength of the transition was well determined against the solar spectrum and accurately reproduced the line-behaviour in Arcturus upon visual examination. One star refers to the second highest level of cleanness, and was assigned to transitions fulfilling the criteria and that to the largest degree were able to reproduce the spectral features (with small discrepancies which may have been caused by continuum placement and uncertainties in the strength of blends). As all the transitions have been critically evaluated, the absence of a star in the 'quality-flag' column is to be interpreted as lines meeting the minimum standards as described in Chapter 3. These act as a complement to the highest quality lines, providing leverage in the extremes of the excitation potential and adding coverage to the equivalent width distribution, both acting so as to break degeneracies and constrain the T_{eff} along with the other θ_* .

Originally, three Fe-linelist were created based on different threshold values of the blend-percentage considered; allowing blends of up to 5%, 20% and 30%. This allowed the change in distribution of line equivalent widths (Figure 4.1) and excitation potentials (Figure 4.2) with increased constrains to be investigated quantitatively. In the following colour-coded Figures (Fig. 4.1, 4.2 and 4.3), any intermediate colour represents the superposition of the colors as indicated by the histogram keys.

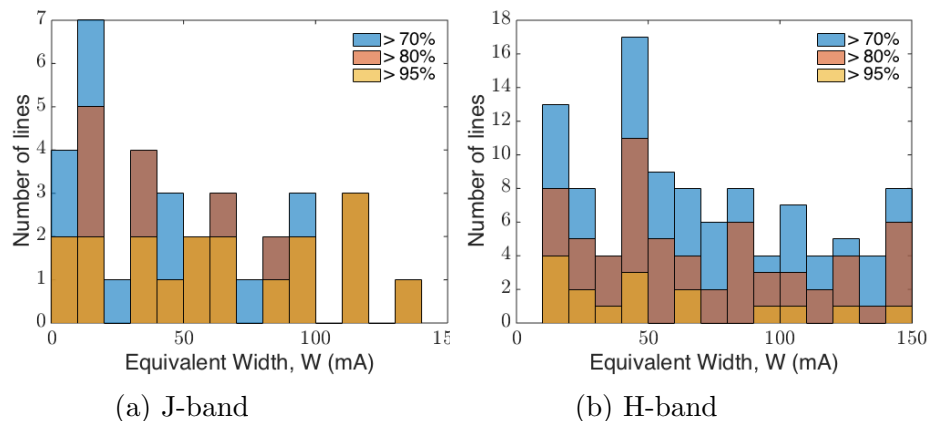


Figure 4.1: Histograms comparing the distribution of equivalent widths for Fe-linelist fulfilling different thresholds on the imposed blend-criteria (30% (blue), 20%(red), 5%(yellow)). Note that the vertical axis in (a) and (b) have different scales.

From Figure 4.1 it can be seen that there is an overall preference towards weaker lines

in both bands, especially when lower threshold values are imposed (blue). This is expected since the selection criteria preferentially selects lines that conform to the weak-line approximation and since most of the NIR transitions originate high up in the term diagram. As higher threshold values on the blend percentage are imposed, this dramatically decreases the number of weakest lines included, whilst maintaining the number of stronger lines unchanged. This makes sense since weaker lines are more sensitive to blends, and will therefore be more sensitive to the threshold values. In the J-band, as depicted in (a), this tightening of the criteria produces a homogenous spread of equivalent width, whilst in the H-band, as depicted in (b), the weak-line bias is maintained. This apparent difference in distributions should not have any immediate effects on the determined T_{eff} of Arcturus. However, if observations of Arcturus-like giants are performed with low SNR or low resolution, this may result in a significant loss of the weak lines needed to determine the temperature.

Figure 4.2 shows the underlying distribution of excitation potentials in the J- and H bands for different selection criteria, following the colour-code as defined for Figure 4.1. The reader should observe that (a) and (b) are plotted on different scales. The distributions are skewed, with a preference towards high excitation potentials, caused by the atomic structure of Fe, with its distribution of energy levels high up in the term diagram that give rise to transitions in the NIR. This is particularly apparent in the H-band (b), an effect that is maintained even when the threshold values are raised. For the temperature determination, this means that the excitation-balance will be weighted unevenly by high- and low excitation potentials. If there is a systematic bias in high or low-excitation lines caused by for example NLTE-effects, this may affect the determined T_{eff} . Purely based on these *a priori* arguments of distributions, the J-band - being more homogenous in terms of equivalent widths and less skewed towards an extreme in excitation potential, has a better potential for determining θ_{\star} .

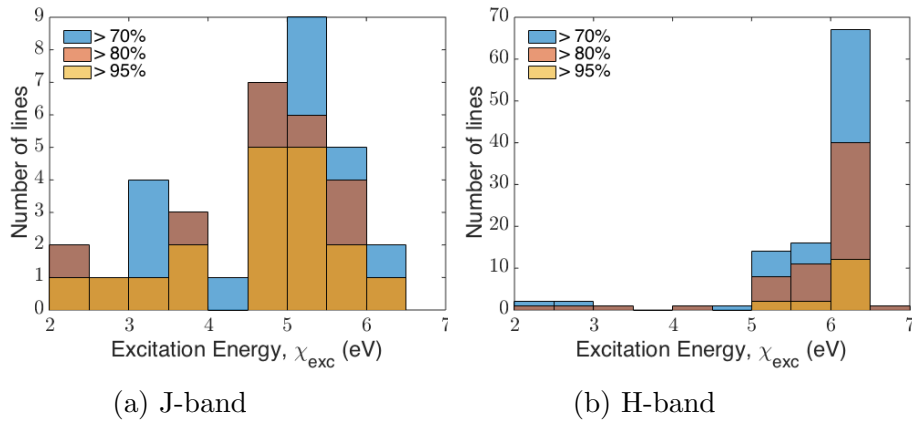


Figure 4.2: Histograms comparing the distribution of excitation potentials, χ_{exc} , for Fe-linelist selections fulfilling different thresholds on the imposed blend-criteria (30% (blue), 20% (red), 5% (yellow)). Note that the vertical axis in (a) and (b) have different scales.

These considerations should however, be weighted against the possibilities as provided by the H-band due to the large number of observed transitions - at least at the cost of reduced threshold values. As an exception to the proclaimed selection criteria, it should be noted that in the 95% cleanness, three transitions ($\lambda 11596.897\text{\AA}$, $\lambda 12217.433\text{\AA}$ and $\lambda 13389.846\text{\AA}$) were added to the line-list because their excitation potentials (5.94, 6.44, 3.02 eV) provided leverage to break degeneracies and constrain the temperature-structure although they did not fulfil the original threshold criteria; the two first having equivalent widths below 5 $m\text{\AA}$, the third not satisfying the threshold blend of 5%.

Figure 4.3 shows how the distribution of excitation potentials of the largest Fe-linelist (allowing for 30% blends) in this thesis compares to that of Jönsson (2014, private communication) in the J (a) and H (b) bands. The intermediate colour denotes the overlapping regimes of the histogram. Jönsson’s linelist is based on the optical spectral region ($\lambda 5800 - 6800\text{\AA}$) and was compiled with selection criteria based on line-strength and the quality of the oscillator strengths, restricting the analysis to experimentally determined values. The linelist that underlies the distribution of Figure 4.3 consists of 39 Fe lines, spanning an excitation potential of 0.9-4.8 eV.

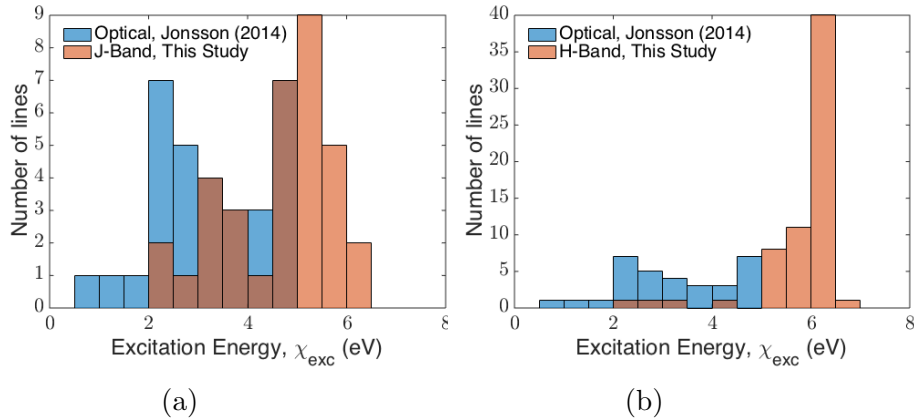


Figure 4.3: Histograms comparing the distribution of excitation potentials, χ_{exc} , in the J- and H band Fe-linelist of this work with Jönsson’s (2014) optical linelist based on a similar method. The J- and H band Fe-linelist plotted allow for 30% blends, the large blend being selected as the threshold values of Jönsson (2014) were not known. Note that the vertical axis in comparison with the J-band (a) and H-band (b) have different scales.

Whilst Jönsson’s linelist indicates a bimodal distribution, the linelist of this work reveals an underlying distribution that is skewed towards higher excitation potentials. The skewness is predicted since NIR transitions originate from energy-levels higher up in the term diagram. Assuming a threshold value that allows for 30% blends, the linelist spans a larger range of excitation potentials, but has low number-counts towards the extremes. Jönsson’s linelist reveals a more even spread. This means Jönsson’s linelist is more robust, and the linelist of this work is more sensitive to loss of lines in the extremes. Correspondingly, this drop in number-counts at the extremities implies that it quickly loses leverage to constrain

Teff. However, as is seen in Figure 4.2, raising the threshold values in the blend-evaluation, even at 80% cleanness, the span in excitation potential is comparable to Jönsson's. Although it could be argued that this is true also at 90%, here, the number of lines is so small that the final parameters become very sensitive to uncertainties with individual lines. It is in a sense, not the excitation span, but the number of lines that prevents better values.

Similar Fe-linelist have been constructed by other groups. Tsantaki et al. (2013) optimised their Fe-linelist by requiring accurate atomic data, equivalent widths of $10 m \text{ \AA} \leq W \leq 200 m \text{ \AA}$ using the optical region ($\lambda 3780 \text{ \AA} - \lambda 6910 \text{ \AA}$). With these criteria in place, a linelist consisting of 299 transitions and spanning an excitation potential of $0.1 - 5 \text{ eV}$ is constructed. Ramírez & Allende Prieto (2011) look for unblended features with well-defined local continuum, and only select lines with reliable gf-values measured in the laboratory. The criteria used in these studies resemble those that this thesis attempts to account for, with a reservation to the use of astrophysical gf-values due to the lack of NIR atomic data.

Resorting to the use of astrophysical gf-values when attempting to retrieve stellar parameters in the NIR is not something that is exclusively done in this thesis. In combination with experimental and theoretical values, APOGEE make use of astrophysical gf-values determined against the Sun and Arcturus (Shetrone et al. 2015). With H-band spectra at high resolution ($R = 22500$), their Fe-lines have been selected based on line-strengths (using opacity at the line-centre as a proxy, with a lower constraint of 0.001 with respect to a normalised continuum to filter out noise) and blends. Due to the large number of Fe I lines observed, Smith et al. (2013) draw a stringent criteria; not to accept *any* blends. In practise, this criteria is achieved by setting the Fe-abundance to zero and excluding the transition from the linelist if a residual line-profile (indicating blends) is apparent.

Smith et al. (2013) claim that the constructed Fe-list spans a range in excitation potential broad enough to constrain Teff. Unfortunately, APOGEE has not published the Fe-linelist. Although the excitation span may provide enough leverage, the stringent blend-criterion excludes Fe-lines with relatively low blends. The results of this work however, indicate that above a certain threshold-value on the cleanness, the blend-percentage does not matter. Rather, it seems like the critical point is to have a large enough *number-count*. This means that APOGEE may rule out lines with small blends that could have proven useful to constrain Teff further. On the other hand, this argument is only justified for Arcturus-like giants. Their stringent criteria may be better for a line-list that aims to work over a large parameter-space.

Table 4.1: Recommended Fe-linelist for the J-band.

λ (Å)	χ_{exc} (eV)	$\log(gf)$ (dex)	Quality
11522.213	3.237	-2.949	
11522.927	5.653	-1.190	★ ★
11572.524	6.280	0.320	★
11596.897	5.943	-0.515	★ ★
11854.240	5.683	-1.704	★
12053.083	4.558	-1.580	★ ★
12119.496	4.593	-1.750	★ ★
12190.099	3.635	-2.600	★ ★
12213.336	4.638	-1.980	★
12217.433	6.440	-0.940	
12227.113	4.607	-1.430	★
12267.889	3.274	-4.190	★
12340.483	2.279	-4.660	★
12342.916	4.638	-1.550	★ ★
12459.764	5.621	-1.570	★
12556.998	2.279	-3.960	★ ★
12648.742	4.607	-1.100	★ ★
12807.152	3.640	-2.630	★ ★
12896.118	4.913	-1.690	★ ★
12934.666	5.393	-1.150	★ ★
13006.685	2.990	-3.340	★ ★
13014.841	5.446	-1.540	★ ★
13039.649	5.655	-1.200	★
13098.877	5.010	-1.610	★
13145.073	4.143	-3.315	
13147.920	5.393	-0.680	
13260.729	5.446	-0.850	★ ★
13291.787	5.478	-1.510	
13352.173	5.309	-0.330	★ ★
13374.700	3.547	-4.133	★
13384.466	3.017	-3.763	
13389.414	5.385	-0.514	★ ★
13389.846	3.018	-4.130	★ ★
13449.422	5.067	-2.000	

Table 4.2: Fe-linelist for the H-band, work in progress.

λ (Å)	χ_{exc} (eV)	$\log(gf)$ (dex)	Quality
14129.144	6.119	0.370	
14158.181	6.218	-0.630	
14166.633	5.446	-1.350	
14169.523	6.453	-0.260	
14331.390	5.393	-0.950	
14408.068	5.446	-2.259	*
14418.662	5.490	-1.818	**
14437.575	4.209	-2.430	*
14460.746	5.064	-1.630	**
14480.606	6.419	0.060	*
14481.907	6.145	0.129	*
14497.822	5.426	-0.302	*
14745.389	2.198	-4.764	
14752.356	5.621	-1.160	
14805.172	6.308	-0.895	**
14808.319	5.385	-1.160	*
14814.735	4.991	-1.112	
14838.276	5.086	-1.936	*
14842.706	6.268	-0.859	*
14866.608	6.252	-0.640	*
14897.408	6.419	0.330	**
14931.854	6.329	-1.020	
14963.761	2.858	-5.088	
14979.698	6.169	-0.450	*
14988.781	6.169	0.225	
15094.697	6.360	0.599	*
15120.509	5.446	-1.4	
15136.127	5.828	-0.481	*
15194.492	2.223	-4.753	*
15230.323	6.419	-1.947	**
15239.715	6.419	-0.067	
15267.025	5.067	-2.325	
15294.904	6.415	-0.181	
15296.163	5.064	-1.870	
15301.560	5.921	-0.650	
15343.788	5.653	-0.570	**
15444.378	6.342	-0.446	**

Continued next page

λ (Å)	χ_{exc} (eV)	$\log(gf)$ (dex)	Quality
15451.301	6.453	-0.435	*
15531.805	6.242	-1.420	*
15537.697	6.323	-0.250	
15542.079	5.642	-0.540	
15566.727	6.350	-0.410	*
15648.510	5.426	-0.560	*
15652.874	6.246	-0.010	*
15656.634	5.874	-2.060	*
15671.006	6.329	-0.510	*
15671.869	5.921	-1.390	
15677.015	6.246	-0.590	*
15677.521	6.246	0.300	
15682.516	6.369	-0.330	
15686.022	6.329	-0.100	
15764.325	6.299	-0.240	*
15764.512	6.252	-0.840	
15816.633	5.956	-0.550	*
15821.712	5.642	-0.770	* *
15837.646	6.303	0.327	*
15854.444	6.474	-0.723	* *
15868.574	6.364	-0.800	
15878.449	5.620	-0.230	*
15891.162	6.306	-0.380	
15891.536	6.306	0.167	*
15894.755	6.206	-0.580	
15896.557	6.342	-0.890	* *
15909.087	6.342	-0.890	*
15909.244	6.342	-0.630	
15920.122	6.258	-0.910	
15929.475	6.308	-0.470	
15929.846	6.258	0.152	*
15941.851	6.360	0.060	
16072.092	5.550	-1.845	*
16072.244	6.350	-0.220	* *
16077.946	2.832	-4.780	*
16115.969	6.390	0.390	*
16156.560	5.956	-0.360	*
16171.933	6.380	-0.440	*
16174.978	6.380	0.300	
16177.994	6.381	-0.470	

Continued next page

λ (Å)	χ_{exc} (eV)	$\log(gf)$ (dex)	Quality
16179.585	6.319	0.200	
16213.004	6.321	-0.440	
16228.655	6.381	-1.140	* *
16246.462	6.275	-0.110	
16284.772	6.398	0.210	
16331.527	5.979	-0.480	*
16440.397	6.286	-0.150	*
16446.553	6.286	-1.740	* *
16494.503	6.369	-0.559	* *
16494.705	6.287	-1.010	* *
16515.671	5.558	-2.530	
16517.226	6.287	0.760	* *
16521.514	6.287	-0.550	*
16522.077	6.287	0.000	*
16551.997	6.411	0.120	
16612.124	5.921	-1.991	*
16612.206	3.397	-4.523	*
16648.203	6.547	-0.450	*
16652.390	6.342	-1.912	*
16661.382	6.342	0.160	
16679.164	5.921	-0.950	*
16721.465	6.380	-0.430	*
16724.688	6.381	-0.660	*
16725.443	6.380	-0.860	*
16782.843	6.347	-1.839	*
16783.040	6.299	-0.810	*

4.3 Arcturus Stellar Parameters

Arcturus is a well studied reference for spectroscopic studies of giant stars, with stellar parameters that have been determined by various groups. Amongst the most recent, Ramírez & Allende Prieto (2011) estimated the values to $T_{\text{eff}} = 4286 \pm 30$ K, $\log g = 1.66 \pm 0.05$ and $[\text{Fe}/\text{H}] = -0.52 \pm 0.04$, the temperature being a weighted average based on observations of blue to mid-infrared (MIR) with $T_{\text{eff}}(\text{visible}) = 4288 \pm 17$ K, $T_{\text{eff}}(\text{NIR}) = 4347 \pm 69$ K, $T_{\text{eff}}(\text{NIR-MIR}) = 4152 \pm 84$ K. These values were confirmed by Smith et al. (2013), who found a temperature $T_{\text{eff}} = 4275 \pm 50$ K. Being the most up-to-date spectroscopic measurements, this thesis makes use of these results as benchmark values.

Using subsets of Fe-lines in Table 4.1 and Table 4.2, linelists with threshold values on the allowed blend-percentage of (30%, 20% and 5%) were constructed. These were used to determine $\theta_{\alpha\text{Boo}}$ for the bands considered. For the J-band, a velocity shift of -30.54 km s^{-1} was added to put the spectrum on laboratory wavelength scale. A macroturbulence $v_{\text{mac}} = 5.53$ km s^{-1} was retrieved using a subset of visually inspected lines. For $T_{\alpha\text{Boo}}$ set as a single free parameter, a grid of initial values gave a final estimate of $T_{\alpha\text{Boo}} = 4287$ K, with a spread of 2 K caused by a variation in T_{init} . Setting the microturbulence as a free parameter - on its own and simultaneously with T_{eff} resulted in a value, stable at $\xi_{\text{mic}} = 1.6$ km s^{-1} together with the previous temperature estimate retrieved. For ξ_{mic} fixed to this value, setting T_{eff} and $[\text{Fe}/\text{H}]$ free, gave $[\text{Fe}/\text{H}]$ at a uniquely determined value of -0.51 dex independent of starting value, and an effective temperature $T_{\text{eff}} = 4298$ K with an insignificant spread of 3 K. It is interesting to note, however, that a small degeneracy seemed to emerge when setting $[\text{Fe}/\text{H}]$ and ξ_{mic} free, resulting in -0.50 and 1.53 respectively. Setting all three $\theta_{\alpha\text{Boo}}$ (T_{eff} , $[\text{Fe}/\text{H}]$ and ξ_{mic}) globally free¹ resulted in values of 4288 K, -0.49 dex and 1.52 km s^{-1} respectively.

Since the methodology relies on a χ^2 -minimisation, the solution to the parameters that minimise the fit is sensitive to how accurately the line-profiles are reproduced. For this reason, an interesting set of SME-jobs were conducted in which v_{mac} was set free together with T_{eff} and $[\text{Fe}/\text{H}]$.² Although this seems counter-productive; v_{mac} having been established unequivocally for fixed $\theta_{\alpha\text{Boo}}$ using a subsample of the highest quality Fe lines, it only conforms to the methodology. The macroturbulence alters the profile by applying a broadening, and in so doing, minimises the fit. Table 4.4 shows a typical set of SME jobs with the input- and output stellar parameters for Arcturus as determined using the different threshold values on the allowed blend-percentage for the J-band, with N indicating the number of lines used for the given sequence, and the additional SME runs with v_{mac} set free. The parameters were varied in a methodological manner to unveil degeneracies.

SME is able to identify a minimum in the χ^2 -plane that is *lower* by increasing the macrotur-

¹The surface gravity, $\log(g)$, was fixed in all SME-jobs due to the lack of Fe II lines.

² ξ_{mic} was fixed to its retrieved value due to its stability and since it is more sensitive to strong lines, for which it had been determined prior.

bulence broadening, an effect that is most pronounced in the set of sequences that use the largest linelist (and hence most lenient on threshold blendness), with a change from 5.53 to 6.16 km s^{-1} . This result does not indicate the presence of a degeneracy in the parameters - v_{mac} only contributes with a broadening to the profile. Rather, it seems to be caused by a combination of too large (*un-carefully* chosen) line-masks for the χ^2 -minimisation to act on, and a large number of lines with $W \leq 20 \text{ m\AA}$ (refer to Figure 4.1) for which off-centre unknown blends may act so as to produce a broadened composite profile. Also, noise in the spectrum tends to broaden weak lines.

The influence of these excessively broadened features on the χ^2 -minimisation would supply the leverage to raise the macroturbulence. This again indicates that the minimised values do not automatically carry physical significance, and must be critically evaluated. For this reason, the $\theta_{\alpha\text{Boo}}$ and v_{mac} as obtained in the discussed SME sequence were ignored in the remaining analysis. Table 4.4 further indicates that T_{eff} systematically decreases with θ_{free} and N ; an effect that the SME compensates for/balances by increasing the metallicity. This correlation is weak enough for T_{eff} and $[\text{Fe}/\text{H}]$ to be determined using a linelist that allows 20% blends, or equivalently; using 24 lines. However, as the number of lines is reduced to 18, things change. When only T_{eff} is set free, the temperature can be retrieved. Despite a low number of lines, this is no real challenge as it is the only free parameter allowed to be varied; and is varied for the highest quality lines only. However, as the metallicity is set free simultaneously, the degeneracy takes over, and without the ability of constraining the slope, results in large departures of retrieved values from literature values.

A major problem with the H-band is that it is a lot denser in terms of spectral features from atoms and molecules, making its analysis a lot more complex. Results for the H-band are therefore a work in progress, with the addition and subtraction of lines continuously being updated, consequently affecting the retrieved values of the stellar parameters. At present, a sub-set of strong high-quality Fe-lines were used to determine a macroturbulence, found to be $v_{\text{mac}} = 5.53 \text{ km s}^{-1}$ and thus in agreement with that found in the J-band. With the linelist, and the values of effective temperature, metallicity and surface gravity fixed to literature values of $T_{\text{eff}} = 4286 \text{ K}$, $\log(g) = 1.66$ and $[\text{Fe}/\text{H}] = -0.52$ a microturbulence of $\xi_{\text{mic}} = 1.73 \text{ km s}^{-1}$ was determined. This is slightly higher than that found in the J-band, but in accordance with what was obtained by Ryde and Jönsson (private communication) and by Ramírez & Allende Prieto (2011) who retrieved a value $\xi_{\text{Ramirez2011}} = 1.74 \text{ km s}^{-1}$. These values are slightly different from that retrieved by Shetrone et al. (2015), who found a value of $\xi_{\text{APOGEE}} = 1.85 \text{ km s}^{-1}$. The effective temperature and metallicity can be retrieved with 105 Fe lines for a threshold-blend set to 30%. For the T_{eff} as the only free parameter, a value of 4279 K is retrieved. Setting it free together with $[\text{Fe}/\text{H}]$ results in values of $4289 \pm 23 \text{ K}$, the spread determined based on the variation caused by T_{init} , and a metallicity constant at -0.48 dex .

Based on these arguments, the conclusion is that the effective temperature, metallicity and microturbulence can be determined spectroscopically using carefully selected iron lines,

assuming a fixed surface gravity determined independently. Whilst blends play a significant role in providing an initial baseline for iron lines, the number of masked lines rather than the threshold value on the blend-percentage contributes most to the determination.

Table 4.3: Arcturus Stellar Parameters, H-band.

Blends (%)	#	glob_ free	Input values [Teff]=K, [Fe/H]=dex, [V _{mac}]	Output values
30	105	Teff	4133	4279
30	105	Teff, [Fe/H]	4186, -0.52 4200, -0.52 4250, -0.52	4274, -0.483 4278, -0.485 4316, -0.483

Table 4.4: Arcturus Stellar Parameters, J-band.

Blends (%)	N	glob_free	Input values	Output values		
			Teff, [Fe/H], v_{mac} (K), (dex), (km s^{-1})	Teff, [Fe/H], v_{mac} (K), (dex), (km s^{-1})		
30	33	Teff	4133	4279		
			4180	4274		
			4286	4276		
			4444	4275		
		Teff, [Fe/H]	4133, -0.52	4259, -0.485		
			4180, -0.52	4262, -0.485		
			4286, -0.52	4272, -0.490		
			4444, -0.52	4270, -0.487		
		Teff, [Fe/H], v_{mac}	4133, -0.52, 5.53	4260, -0.436, 6.16		
			4180, -0.52, 5.53	4260, -0.437, 6.16		
			4286, -0.52, 5.53	4262, -0.437, 6.17		
			4444, -0.52, 5.53	4262, -0.438, 6.16		
		20	24	Teff	4133	4259
					4180	4260
					4286	4258
					4444	4262
Teff, [Fe/H]	4133, -0.52			4231, -0.464		
	4180, -0.52			4232, -0.464		
	4286, -0.52			4236, -0.465		
	4444, -0.52			4237, -0.467		
Teff, [Fe/H], v_{mac}	4133, -0.52, 5.53			4231, -0.420, 6.03		
	4180, -0.52, 5.53			4230, -0.420, 6.03		
	4286, -0.52, 5.53			4230, -0.420, 6.03		
	4444, -0.52, 5.53			4231, -0.420, 6.03		
5	18			Teff	4133	4248
					4180	4233
					4286	4246
					4444	4236
		Teff, [Fe/H]	4133, -0.52	4125, -0.421		
			4180, -0.52	4125, -0.421		
			4286, -0.52	4126, -0.421		
			4444, -0.52	4126, -0.421		
		Teff, [Fe/H], v_{mac}	4133, -0.52, 5.53	4135, -0.380, 6.03		
			4180, -0.52, 5.53	4134, -0.380, 6.03		
			4286, -0.52, 5.53	4135, -0.380, 6.03		
			4444, -0.52, 5.53	4135, -0.380, 6.03		

4.4 Uncertainties in Teff

Several sources of errors contribute to produce uncertainties in the determined effective temperature. Since spectrum synthesis minimises the difference between synthetic and empirical spectra, all of the parameters involved - as well as model assumptions, should in theory affect the determined value of θ_{free} . Qualitatively, these include uncertainties caused by

- **gf-values:** If oscillator strengths are determined computationally, uncertainties are introduced by simplifying approximations/assumptions, for example by using perturbation theory. Experimentally, uncertainties arise from the signal-to-noise ratio, normalisation, calibration and precision of the detector. Astrophysical gf-values will introduce uncertainties associated with continuum-mask placement - which in itself makes the gf-values sensitive to the signal-to-noise ratio. Further, the astrophysical determination truncates NLTE and 3D effects, which will alter the gf-values systematically.
- θ_{\star} : Since spectrum synthesis solves the stellar parameters simultaneously, the parameters are correlated. Therefore, uncertainties in one of them can propagate into the others.
- **continuum-masks (*cmasks*):** The placement of continuum masks influences the local continuum around a line. Since the line-strength is measured against the continuum level (preferably normalised to unity), the selected continuum masks directly influence the determined stellar parameter. Accordingly, errors/uncertainties in continuum placement propagate to errors in the determined θ_{star} .
- **line-masks (*lmask*):** The lmask define the regions across which the χ^2 -minimisation acts. Therefore the lmask must be chosen with care, so as to avoid bad/hot pixels, telluric artefacts.
- **Model assumptions:** Uncertainties associated with the model can be subdivided into those concerning (i) *the model structure (atmospheric model)*, and (ii) *line-strengths and line-profiles*. (i) refers to NLTE and 3D effects that alter the temperature, pressure and density structures of the photosphere. Both of these can generate systematic errors, but since it is model dependent it will only be important to consider when parameters as determined using different methodologies are compared.
- θ_{init} : The χ^2 -minimisation works by searching through the parameter-space and evaluating in what direction to step in order to improve the fit. This evaluation depends on the slope of the χ^2 -surface. The method evaluates the slope based on a finite reach in the grid-search, in turn based on the current position in the plane. Concerns include θ_{init} causing the method to move in the wrong direction if only

small gradients are present; and getting stuck in *local* minima rather than retrieving the *global* minimum.

- **Resolution (R) and Signal-to Noise (SNR):** Reducing the resolution implies that fewer structures are resolved, which consequently gives rise to more blends within a spectral feature. This is increasingly so for weak lines, which in itself may provide a problem since the excitation balance of Fe-lines relies heavily on these weak lines. Similarly, *noise* makes continuum placement difficult, which, again, becomes more severe for weaker lines. Apart from noise intrinsically connected to the detected signal, dividing the stellar by the telluric spectrum introduces further noise.

For determining θ_* of other stars, the resolution and SNR may cause large uncertainties. However, since the line-list is optimised for Arcturus using a high resolution ($R = 100,000$) Atlas, uncertainties associated with these effects will be negligible in comparison to those associated with other sources. Likewise, uncertainties and systematic errors associated with the model assumptions only become important for the comparison of stellar parameters as retrieved with different methodologies, and when applying the astrophysically determined gf-values on stars that span a different grid of stellar parameters. Although Arcturus is only slightly sub-solar in metallicity, it could be invoked that the model-assumptions would cause a systematic effect of the determined parameters of Arcturus. However, the fact that the 3D and NLTE effects are negligible (refer to Section 2.2 & 2.3) for Arcturus θ_* , and since Fe lines that do not reproduce Arcturus spectral features are actively removed from the Fe-linelist, these uncertainties should be negligible too.

The effects of lmask and cmask on the retrieved effective temperature (Table 4.5 and Table 4.6 respectively) is investigated by varying mask limits and mask placement for different lines in a systematic manner. The retrieved temperatures are compared to a 'benchmark temperature' ($T_{\text{benchmark}}$), which corresponds to the effective temperature as retrieved for $\theta_{\text{free}} = T_{\text{eff}}$ for the defined line-list with ideal mask placements. To reduce the impact of individual lmask and pairs of cmask, the measurements are repeated N times, varying the masks. This procedure is repeated for different numbers of altered lmask and cmask.

One of the major concerns is how to go about varying the masks. This cannot be conducted straight off according to some Monte-Carlo scheme as continuum and line masks tend to be selected by careful examination. To avoid bias caused by knowledge of prior mask-placements, the spectra were re-synthesised without masks. Upon visual examination, new masks were defined as ideally as possible.

Table 4.5: Temperature differences induced by line-mask placement. ΔT and σ are calculated based on N=4 measurements.

Blends (%)	#	Bechmark Teff [K]	Number of Altered l masks	ΔT [K]	σ [K]
30	33	4263	1	2	1
			5	5	9
			10	14	12
			15	16	12
20	24	4272	1	3	8
			5	9	8
			10	11	13
			15	1	6
5	18	4231	1	31	21
			5	6	4
			10	1	3
			15	-5	3

Table 4.6: Temperature differences induced by continuum-mask placement. ΔT and σ are calculated based on N=4 measurements.

Blends (%)	#	Bechmark Teff [K]	Number of Altered cmasks	ΔT [K]	σ [K]
30	33	4263	1	-4	12
			10	-16	32
20	24	4272	1	-2	18
			10	-34	22
5	18	4231	1	1	2
			10	51	29

For a temperature measurement T_i obtained in an SME-job, the mean difference ΔT and the spread σ of the N measurements in a sequence are calculated according to

$$\Delta T = \frac{1}{N} \sum_i^N (T_{\text{benchmark}} - T_i), \quad (4.1)$$

and

$$\sigma = \sqrt{\frac{1}{N} \sum_i^N (T_{\text{benchmark}} - T_i)^2} \quad (4.2)$$

to get quantitative measures of systematic offsets and the uncertainty in the sequence.

The local environment around the Fe-line for which the lmask and the cmasks are varied can have a large impact on the derived temperature, mostly caused by difficulties in defining a continuum. The uncertainty in temperature arising from variations in lmask and cmasks are both observed to depend on the number of lines in the Fe-linelist being used, and on the number of masks that are altered. These results are predicted; in a larger linelist one lmask or one set of cmasks will carry less statistical weight for the χ^2 -evaluation, making it less sensitive to small fluctuations. In order to get a temperature difference, more masks therefore have to be altered. It is interesting to note that whilst ΔT_{lmask} is biased towards positive values (meaning that the varied masks give rise to a lower temperature estimate), alterations in the cmasks tend to cause ΔT_{cmask} to become negative, and therefore the temperature estimate to overshoot the benchmark value. There is no reason why such systematic offsets towards positive or negative values should be obtained based on the masks. If anything, it may only testify to the low statistics in which case it should not be overanalysed. It does however give an indication of the uncertainties in the values, which are relatively low for lmask, but become increasingly important to account for cmask when using few lines.

With the same nomenclature with regards to systematic offsets and spread in the retrieved values, the propagation of uncertainties associated with the gf-values on to Teff are investigated. This was done by identifying an Fe-line with an astrophysically determined gf-value in the solar spectrum. The gf-value was then manually varied until a difference between the optimised and manually varied value was evident. A change of 0.02 dex gave a subtle but unambiguous difference,³ and was taken to be a measure of the 1σ confidence interval. Assuming that the uncertainty in the astrophysical gf-values follow a normal distribution, an IDL script was constructed which added Gaussian-distributed noise (with the standard deviation taken to be 0.02 dex) to all of the Fe lines in the linelist. In a “small-number statistics” Monte-Carlo scheme, Fe-linelist with the added uncertainties were regenerated and used to retrieve Teff. The resulting temperatures for the different sequences and line-lists are shown in Table B.1 (Appendix B), whilst the spreads and mean differences have been compiled in Table 4.7.

³At 0.01 dex difference a small change may have been visible. However, since I was biased towards observing a difference, the decision was taken to use a difference of 0.02 dex.

Table 4.7: Temperature differences induced by gaussian-distributed uncertainties in gf-values assuming $1\sigma = 0.02$, with ΔT and σ calculated based on $N = 21$ measurements.

Blends (%)	#	Benchmark Teff [K]	ΔT [K]	σ [K]
30	33	4263	9	38
20	24	4272	48	50
5	18	4231	21	33

The inconsistent trend of ΔT in Table 4.7 indicates that the systematic offsets have not converged, and that the statistics are too small to draw a final conclusion based on the obtained results. However, the spread is an indication that the uncertainties in effective temperature propagated from uncertainties in astrophysically determined gf-values must be accounted for.

To quantify a total uncertainty in Teff the uncertainties in gf-values, lmask and cmask are considered to be statistically uncorrelated.⁴ Adding the uncertainties in quadrature:

$$\sigma_{\text{Teff}} = \left(\sigma_{\text{lmask}}^2 + \sigma_{\text{cmask}}^2 + \sigma_{\text{gf}}^2 + \sigma_{\text{init}}^2 \right)^{1/2}, \quad (4.3)$$

where the subscripts “lmask”, “cmask”, “gf” and “init” denote line-masks, continuum-masks, gf-values and initial input accordingly. With the most conservative uncertainty estimates, this gives:

$$\sigma_{\text{Teff}}(70\%, \text{J-band}) \sim \pm 50 \text{ K},$$

$$\sigma_{\text{Teff}}(80\%, \text{J-band}) \sim \pm 60 \text{ K},$$

$$\sigma_{\text{Teff}}(95\%, \text{J-band}) \sim \pm 50 \text{ K},$$

and

$$\sigma_{\text{Teff}}(70\%, \text{H-band}) \sim \pm 60 \text{ K},$$

where σ_{init} was neglected for the J-band in reference to the grid of starting values conducted (refer to Section 4.3 and Table 4.4), and was estimated to contribute with an uncertainty of $\sigma_{\text{init}} = \pm 23 \text{ K}$ based on the retrieved temperature estimates of Table 4.3.

⁴This assumption is questionable since continuum level and line masks have to be defined when solving astrophysical gf-values. However, since gf-values were solved against the Sun, and the uncertainties in cmask and lmask are based on Arcturus, the assumption may be justified.

Chapter 5

Conclusion

5.1 Summary

In this thesis, iron lines in the J- and H atmospheric transmission bands have been successfully used to spectroscopically determine the effective temperature of the cool giant, Arcturus. The method consisted of subjecting Fe lines to a “blend-evaluation”, with the evaluation giving an output in the form of a blend-percentage. A threshold value on the blend-percentage and constraints on the strength of the line acted as a preliminary proxy for how useful an Fe-line was in the determination of stellar parameters. Since the stellar parameters were determined by spectrum synthesis, good gf-values were required to synthesise the lines and reproduce the empirical spectrum. The absence of experimentally determined gf-values, and the uncertainties involved with theoretical values motivated the calculation of astrophysical gf-values against the Sun. These were used as input in the blend-evaluation and spectrum synthesis of Arcturus to retrieve its stellar parameters.

The astrophysically determined gf-values were observed to follow a one-to-one correspondence with experimental data (where these have been measured). The methodology of excitation-balance of Fe lines to obtain stellar parameters was verified by successfully retrieving the Solar values for the effective temperature and metallicity, with parameters of $T_{\text{eff}\odot} = 5767$ K and $[\text{Fe}/\text{H}]_{\odot} = -0.005$ dex in the J-band, and $T_{\text{eff}\odot} = 5780$ K and $[\text{Fe}/\text{H}]_{\odot} = -0.01$ dex in the H-band assuming a fixed surface gravity for both bands. Arcturus stellar parameters could be retrieved to good agreement with literature values using 24 lines (and a blend-threshold of 20%), assuming fixed surface gravity. In the J-band, a version of this linelist gave resulting values of $T_{\text{eff}\alpha\text{Boo}} = 4288$ K, $[\text{Fe}/\text{H}]_{\alpha\text{Boo}} = -0.49$ dex and $\xi_{\text{mic}} = 1.52$ when set free simultaneously. The result is in agreement with literature values. Due to more spectral features and interfering molecules, the values were harder to retrieve in the H-band, and the temperature determination showed a spread of ± 20 K depending on the assumed initial value of Teff. Although the H-band remains a work in progress, preliminary results indicate retrieved temperatures and metallicities of $T_{\text{eff}\alpha\text{Boo}} \sim 4280$ K and $[\text{Fe}/\text{H}]_{\alpha\text{Boo}} = -0.48$ dex.

In an attempt to quantify the uncertainties in the obtained T_{eff} , line- and continuum masks were re-defined, and T_{eff} reevaluated. To quantify uncertainties associated with the astrophysical gf -values, a small Monte-Carlo scheme was constructed which added a Gaussian-distributed noise to each Fe-line. An estimate of the uncertainty in T_{eff} caused by uncertainties in gf -values was obtained by re-evaluating T_{eff} using the perturbed gf -values. Assuming the sources of uncertainties to be statistically independent, these were added in quadrature to produce total uncertainties of the order ± 55 K.

The results of this thesis demonstrate that the NIR spectral region has a large potential for the spectroscopic determination of stellar parameters of Arcturus-like giants using excitation balance of Fe-lines.

5.2 Future Prospects

With an outset in this thesis, several paths could be pursued. One path to go concerns the stability and the statistics of the Fe-linelist constructed. Using a large Monte-Carlo scheme, one could imagine the removal of randomly selected lines, and redetermining the stellar parameters. By systematically removing more and more lines, the robustness of the linelist could be tested. One could further imagine this scheme to be implemented so as to allow the inclusion of uncertainties in gf -values, and alterations in continuum- and line-masks according to the uncertainty-calculations performed above.

A second approach would be to apply the linelists to a sample of cool standard stars, to see if their parameters can be retrieved. The major limitation with this approach is the lack of high-resolution NIR spectra.

Other paths could consist of extending the analysis by constructing linelists for the K, L and M atmospheric bands, or to experimentally determine oscillator strengths for transitions in the NIR.

Bibliography

- Asplund, M. 2005, *ARA&A*, 43, 481
- Asplund, M., Grevesse, N., Sauval, A. J., & Scott, P. 2009, *ARA&A*, 47, 481
- Barklem, P. S. & Piskunov, N. 2003, in *IAU Symposium*, Vol. 210, *Modelling of Stellar Atmospheres*, ed. N. Piskunov, W. W. Weiss, & D. F. Gray, 28P
- Bergemann, M., Lind, K., Collet, R., & Asplund, M. 2011, *Journal of Physics Conference Series*, 328, 012002
- Bergemann, M., Lind, K., Collet, R., Magic, Z., & Asplund, M. 2012, *MNRAS*, 427, 27
- Biemont, E., Palmeri, P., & Quinet, P. 1999, *Astrophysics and Space Science*, 269
- Böhm-Vitense, E. 1989, *Introduction to stellar astrophysics*. Vol. 2. *Stellar atmospheres*.
- Collet, R., Asplund, M., & Trampedach, R. 2007, *A&A*, 469, 687
- Collet, R., Magic, Z., & Asplund, M. 2011, *Journal of Physics Conference Series*, 328, 012003
- Cowan, R. D. 1981, *The theory of atomic structure and spectra*
- Gilmore, G., Randich, S., Asplund, M., et al. 2012, *The Messenger*, 147, 25
- Goldman, A., Schoenfeld, W. G., Goorvitch, D., et al. 1998, *jqsr*, 59, 453
- Goorvitch, D. 1994, *apjs*, 95, 535
- Gray, D. F. 2008, *The Observation and Analysis of Stellar Photospheres*
- Gustafsson, B., Edvardsson, B., Eriksson, K., et al. 2008, *A&A*, 486, 951
- Hayek, W., Asplund, M., Collet, R., & Nordlund, Å. 2011, *A&A*, 529, A158
- Heiter, U., Barklem, P., Fossati, L., et al. 2008, *J. Phys. Conf. Ser.*, 130, 012011
- Henry, L., Vardya, M. S., & Bodenheimer, P. 1965, *ApJ*, 142, 841

- Holtzman, J. A., Shetrone, M., Johnson, J. A., et al. 2015, ArXiv e-prints
- Hourihane, A. P., Gilmore, G. G., Randich, S., Worley, C. C., & Gaia-ESO Consortium. 2014, in *Astronomical Society of India Conference Series*, Vol. 11, Astronomical Society of India Conference Series, 175–182
- Jorgensen, U. G. & Larsson, M. 1990, *A&A*, 238, 424
- Jorgensen, U. G., Larsson, M., Iwamae, A., & Yu, B. 1996, *A&A*, 315, 204
- Kupka, F., Piskunov, N., Ryabchikova, T., Stempels, H., & Weiss, W. 1999, *aaps*, 138, 119
- Kurucz, R. L. 1988, *Trans. IAU, XXB*, M. McNally, ed., Dordrecht: Kluwer, 168
- Kurucz, R. L. 2006, Robert L. Kurucz on-line database of observed and predicted atomic transitions
- Kurucz, R. L. 2007, Robert L. Kurucz on-line database of observed and predicted atomic transitions
- Kurucz, R. L. & Peytremann, E. 1975, *SAO Special Report*, 362, 1, (KP)
- Lind, K., Bergemann, M., & Asplund, M. 2012, *Mon. Not. R. Astron. Soc.*, 427, 50
- Livingston, W. & Wallace, L. 1991, *An atlas of the solar spectrum in the infrared from 1850 to 9000 cm⁻¹ (1.1 to 5.4 micrometer)*
- Mashonkina, L., Gehren, T., Shi, J.-R., Korn, A. J., & Grupp, F. 2011, *A&A*, 528, A87
- Niemczura, E., Smalley, B., & Pych, W. 2014, *Determination of Atmospheric Parameters of B-, A-, F- and G-Type Stars Lectures from the School of Spectroscopic Data Analyses*
- Nordlund, A. & Dravins, D. 1990, *A&A*, 228, 155
- Nordlund, Å., Stein, R. F., & Asplund, M. 2009, *Living Reviews in Solar Physics*, 6, 2
- O'Brian, T. R., Wickliffe, M. E., Lawler, J. E., Whaling, W., & Brault, J. W. 1991, *Journal of the Optical Society of America B Optical Physics*, 8, 1185, (BWL)
- Oh, H., Pak, S., Yuk, I., et al. 2010, in *American Astronomical Society Meeting Abstracts*, Vol. 216, American Astronomical Society Meeting Abstracts 216, 415.10
- Oliva, E., Tozzi, A., Ferruzzi, D., et al. 2014, in *Society of Photo-Optical Instrumentation Engineers (SPIE) Conference Series*, Vol. 9147, Society of Photo-Optical Instrumentation Engineers (SPIE) Conference Series, 7
- Origlia, L., Oliva, E., Baffa, C., et al. 2014, in *Society of Photo-Optical Instrumentation Engineers (SPIE) Conference Series*, Vol. 9147, Society of Photo-Optical Instrumentation Engineers (SPIE) Conference Series, 1

- Origlia, L., Oliva, E., Maiolino, R., et al. 2013, SIMPLE: a high-resolution near-infrared spectrograph for the E-ELT
- Piskunov, N. E., Kupka, F., Ryabchikova, T. A., Weiss, W. W., & Jeffery, C. S. 1995, *A&A*, 112, 525
- Querci, F., Querci, M., & Kunde, V. G. 1971, *A&A*, 15, 256
- Quinet, P. & Biemont, E. 2004, *Atomic Data and Nuclear Tables* 87, 207
- Raassen, A. J. J. & Uylings, P. H. M. 1998, *A&A*, 340, 300, (RU)
- Ramírez, I. & Allende Prieto, C. 2011, *Astrophys. J.*, 743, 135
- Ruchti, G. R., Bergemann, M., Serenelli, A., Casagrande, L., & Lind, K. 2013, *MNRAS*, 429, 126
- Ruffoni, M. P., Allende Prieto, C., Nave, G., & Pickering, J. C. 2013, *Astrophys. J.*, 779, 17
- Ruffoni, M. P., Den Hartog, E. A., Lawler, J. E., et al. 2014, *MNRAS*, 441, 3127
- Ryde, N. & Schultheis, M. 2015, *A&A*, 573, A14
- Seaton, M. J., Yan, Y., Mihalas, D., & Pradhan, A. K. 1994, *MNRAS*, 266, 805
- Shetrone, M., Bizyaev, D., Lawler, J., et al. 2015, *ArXiv e-prints*
- Smith, V. V., Cunha, K., Shetrone, M. D., et al. 2013, *ApJ*, 765, 16
- Tsantaki, M., Sousa, S. G., Adibekyan, V. Z., et al. 2013, *A&A*, 555, A150
- Valenti, J. & Piskunov, N. 1996, *aaps*, 118, 595
- Valenti, J., Piskunov, N., & Heiter, U. 2012, *Spectroscopy Made "Easy" (SME) User Handbook*

Appendix A

Astrophysical gf-values

Table A.1: Astrophysical gf-values

χ_{exc} (eV)	λ (Å)	$\log(gf)_{VALD}$	$\log(gf)_{astph}$	$\Delta \log(gf)$	σ
2.198	14745.389 _H	-5.100 ^a	-4.764	-0.336	
	15490.339 _H	-4.574 ^e	-4.714	0.140	
2.223	11593.589 _J	-2.448 ^e	-2.420	-0.028	
	15194.492 _H	-4.808 ^a	-4.753	-0.055	
2.279	12340.483 _J	-5.122 ^a	-4.660	-0.462	
	12556.998 _J	-3.626 ^e	-3.960	0.334	
	12879.768 _J	-3.458 ^e	-3.460	0.002	0.400
2.424	14729.553 _H	-4.708 ^a	-4.550	-0.158	
2.832	15077.241 _H	-4.092 ^a	-4.080	-0.012	
2.990	13006.685 _J	-3.722 ^a	-3.340	-0.382	
3.252	12946.532 _J	-4.760 ^a	-4.220	-0.540	
3.274	12267.889 _J	-4.370 ^a	-4.190	-0.180	
3.415	14659.029 _H	-3.891 ^a	-3.830	-0.061	
	15611.146 _H	-3.765 ^a	-2.950	-0.815	
3.547	11681.594 _J	-3.611 ^a	-3.384	-0.227	

Continued next page

APPENDIX A. ASTROPHYSICAL GF-VALUES

χ_{exc} (eV)	λ (Å)	$\log(gf)_{VALD}$	$\log(gf)_{astph}$	$\Delta \log(gf)$	σ
3.635	12190.099 _J	-2.330 ^e	-2.600	0.270	
3.640	12807.152 _J	-2.630 ^a	-2.630	0.000	
4.076	14806.005 _H	-3.033 ^a	-3.332	0.299	
4.260	14668.347 _H	-3.041 ^a	-3.074	0.033	
	15360.236 _H	-2.702 ^a	-2.760	0.058	
4.284	15095.197 _H	-2.769 ^a	-2.729	-0.040	
4.558	12053.083 _J	-1.543 ^e	-1.580	0.037	
4.559	12638.705 _J	-0.774 ^a	-0.720	-0.054	
	15629.624 _H	-3.038 ^a	-3.038	0.000	
4.580	11594.548 _J	-1.882 ^a	-2.030	0.148	
4.593	12119.496 _J	-1.637 ^a	-1.750	0.113	
4.607	12227.113 _J	-1.354 ^a	-1.430	0.076	
	12648.742 _J	-1.140 ^e	-1.100	-0.040	
4.638	12213.336 _J	-1.829 ^a	-1.980	0.151	
	12342.916 _J	-1.449 ^a	-1.550	0.101	
	12615.928 _J	-1.505 ^a	-1.640	0.135	0.026
4.913	12896.118 _J	-1.426 ^a	-1.690	0.264	
4.956	12510.519 _J	-1.604 ^a	-1.950	0.346	
4.988	12512.240 _J	-2.292 ^a	-2.440	0.148	
	13286.814 _J	-1.103 ^a	-3.597	2.494	
5.010	13098.877 _J	-1.289 ^a	-1.610	0.321	
5.020	12933.006 _J	-1.547 ^a	-1.850	0.303	
5.033	14737.574 _H	-1.338 ^a	-1.400	0.062	

Continued next page

APPENDIX A. ASTROPHYSICAL GF-VALUES

χ_{exc} (eV)	λ (Å)	$\log(gf)_{VALD}$	$\log(gf)_{astph}$	$\Delta \log(gf)$	σ
	15593.750 _H	-1.923 ^a	-1.850	-0.073	
5.064	14460.746 _H	-1.518 ^a	-1.630	0.112	
	15296.163 _H	-1.783 ^a	-1.870	0.087	
5.067	13449.422 _J	-1.764 ^a	-2.000	0.236	
	14956.570 _H	-1.263 ^a	-1.350	0.087	
	15267.025 _H	-2.147 ^a	-2.325	0.178	
	15854.029 _H	-2.030 ^a	-2.500	0.470	
	16578.064 _H	-1.977 ^d	-2.880	0.903	0.327
5.086	14243.917 _H	-1.692 ^a	-1.710	0.018	
	14838.276 _H	-1.770 ^a	-1.936	0.166	
5.100	14476.050 _H	-1.948 ^a	-2.006	0.058	
5.106	15676.585 _H	-2.006 ^a	-1.870	-0.136	
	16665.387 _H	-2.152 ^a	-2.152	0.000	
5.112	16822.691 _H	-2.070 ⁱ	-3.070	1.000	
5.273	11602.910 _J	-1.961 ^a	-2.001	0.040	
	12670.169 _J	-1.877 ^a	-2.140	0.263	
5.309	13352.173 _J	-0.513 ^a	-0.330	-0.183	
5.352	12729.963 _J	-2.194 ^a	-2.140	-0.054	
	16153.247 _H	-0.680 ^a	-0.600	-0.080	
5.385	12580.192 _J	-2.392 ^a	-2.110	-0.282	
	14808.319 _H	-1.377 ^a	-1.160	-0.217	
	15692.747 _H	-0.378 ^a	-0.350	-0.028	
	16324.452 _H	-0.551 ^a	-0.410	-0.141	0.109
5.393	12733.769 _J	-2.022 ^a	-2.100	0.078	
	12934.666 _J	-0.907 ^a	-1.150	0.243	
	13147.920 _J	-0.830 ^a	-0.680	-0.150	
	14331.390 _H	-0.940 ^e	-0.950	0.010	0.163
5.410	14294.260 _H	-0.594 ^a	-0.572	-0.022	

Continued next page

APPENDIX A. ASTROPHYSICAL GF-VALUES

χ_{exc} (eV)	λ (Å)	$\log(gf)_{VALD}$	$\log(gf)_{astph}$	$\Delta \log(gf)$	σ
	15682.017 _H	-1.750 ^a	-2.130	0.380	
	16198.503 _H	-0.440 ^a	-0.340	-0.100	0.258
5.426	14565.938 _H	0.094 ^a	0.155	-0.061	
	15648.510 _H	-0.596 ^a	-0.560	-0.036	
	16009.611 _H	-0.467 ^a	-0.350	-0.117	0.042
5.446	13014.841 _J	-1.683 ^a	-1.540	-0.143	
	13260.729 _J	-0.642 ^e	-0.850	0.208	
	13487.505 _J	-1.723 ^a	-1.550	-0.173	
	14166.633 _H	-1.788 ^a	-1.350	-0.438	
	14408.068 _H	-1.869 ^a	-2.259	0.390	
	14946.743 _H	-1.567 ^a	-1.270	-0.297	0.314
5.478	13291.787 _J	-2.807 ^a	-1.510	-1.297	
5.485	15921.096 _H	-0.915 ^e	-1.410	0.495	
5.491	15159.669 _H	-1.843 ^a	-1.843	0.000	
5.507	15229.279 _H	-2.072 ^a	-2.243	0.171	
5.538	14405.226 _H	-1.143 ^a	-1.492	0.349	
	16566.732 _H	-1.961 ⁱ	-2.400	0.439	
5.539	14251.264 _H	-1.085 ^a	-0.490	-0.595	
	14956.152 _H	0.102 ^a	0.227	-0.125	
5.558	16515.671 _H	-2.103 ⁱ	-2.530	0.427	
5.587	12667.114 _J	-1.484 ^a	-1.510	0.026	
	14523.618 _H	-0.350 ^a	-0.770	0.420	
	15077.287 _H	-0.049 ^a	-0.750	0.701	
	15244.974 _H	-0.268 ^a	0.227	-0.495	
	15858.657 _H	-1.151 ^a	-1.190	0.039	
	16619.738 _H	-0.802 ⁱ	-1.550	0.748	0.475
5.607	16018.725 _H	-1.983 ^a	-1.840	-0.143	
	16460.368 _H	-2.026 ^a	-1.880	-0.146	

Continued next page

APPENDIX A. ASTROPHYSICAL GF-VALUES

χ_{exc} (eV)	λ (Å)	$\log(gf)_{VALD}$	$\log(gf)_{astph}$	$\Delta \log(gf)$	σ
5.614	15812.783 _H	-2.076 ^a	-1.940	-0.136	
5.621	11682.253 _J	-3.419 ^a	-1.335	-2.084	
	11755.989 _J	-1.733 ^a	-1.770	0.037	
	12459.764 _J	-1.436 ^a	-1.570	0.134	
	14752.356 _H	-0.775 ^a	-1.160	0.385	
	15120.018 _H	-1.877 ^a	-2.536	0.659	
	15122.380 _H	-0.215 ^a	-0.289	0.074	
	15395.718 _H	-0.113 ^a	-0.104	-0.009	
	15723.586 _H	0.334 ^a	0.334	0.000	
	15906.044 _H	-0.149 ^a	0.080	-0.229	
	16586.051 _H	-0.647 ^d	-1.480	0.833	
	15394.673 _H	0.006 ^a	0.006	0.000	0.755
5.642	11620.567 _J	-1.664 ^a	-1.626	-0.038	
	15144.051 _H	-0.402 ^a	-0.520	0.118	
	15531.752 _H	-0.236 ^a	-0.390	0.154	
	15534.245 _H	-0.384 ^a	-0.150	-0.234	
	15542.079 _H	-0.336 ^a	-0.540	0.204	
	15821.712 _H	-0.814 ^a	-0.770	-0.044	
	16333.141 _H	-0.602 ^a	-1.360	0.758	0.314
5.653	11522.927 _J	-1.190 ^a	-1.190	0.000	
	11585.210 _J	-1.301 ^a	-1.220	-0.081	
	15343.788 _H	-0.582 ^a	-0.570	-0.012	
	15741.918 _H	-0.106 ^a	-0.106	0.000	0.039
5.655	13039.649 _J	-0.726 ^a	-1.200	0.474	
	13222.525 _J	-1.273 ^a	-1.640	0.367	
5.669	12475.829 _J	-1.583 ^a	-1.660	0.077	
	13107.974 _J	-1.453 ^a	-1.840	0.387	
5.683	11854.240 _J	-1.305 ^a	-1.704	0.399	
5.693	11568.336 _J	-1.688 ^a	-1.610	-0.078	
	12010.579 _J	-1.169 ^a	-1.551	0.382	
5.699	11725.563 _J	-1.101 ^a	-1.522	0.421	

Continued next page

APPENDIX A. ASTROPHYSICAL GF-VALUES

χ_{exc} (eV)	λ (Å)	$\log(gf)_{VALD}$	$\log(gf)_{astph}$	$\Delta \log(gf)$	σ
5.793	15524.311 _H	-0.864 ^a	-1.359	0.495	
	15537.456 _H	-1.068 ^a	-1.670	0.602	
5.796	14650.679 _H	-1.696 ^a	-1.463	-0.233	
5.814	14576.767 _H	-2.036 ^a	-1.135	-0.901	
	15940.920 _H	-1.641 ^a	-1.320	-0.321	
5.828	15136.127 _H	-0.179 ^a	-0.481	0.302	
	15662.016 _H	0.382 ^a	0.390	-0.008	
	16807.438 _H	-1.147 ^d	-1.410	0.263	0.169
5.829	14385.648 _H	-1.627 ^a	-1.684	0.057	
	15259.366 _H	-1.232 ^a	-1.694	0.462	
5.872	16910.686 _H	-1.618 ^f	-1.790	0.172	
5.874	14323.863 _H	-1.501 ^a	-1.679	0.178	
	15604.167 _H	-1.174 ^a	-1.180	0.006	
	15656.634 _H	-1.280 ^a	-2.060	0.780	
	15911.305 _H	0.175 ^a	0.175	0.000	
	16799.651 _H	-1.384 ^a	-0.420	-0.964	
	16843.231 _H	-1.143 ⁱ	-1.270	0.127	0.563
5.900	15908.558 _H	-1.607 ^a	-1.680	0.073	
5.913	15277.062 _H	-1.517 ^a	-1.629	0.112	
5.921	15143.092 _H	-1.309 ^a	-1.309	0.000	
	15176.715 _H	-0.686 ^a	-0.766	0.080	
	15301.560 _H	-0.625 ^a	-0.650	0.025	
	15671.869 _H	-1.218 ^a	-1.390	0.172	
	15901.521 _H	-1.251 ^a	-0.440	-0.811	
	15964.867 _H	0.136 ^a	0.080	0.056	
	16235.969 _H	0.002 ^a	-0.230	0.232	
	16292.843 _H	-0.099 ^a	-0.470	0.371	
	16318.693 _H	-3.139 ^a	-0.420	-2.719	
	16398.170 _H	0.208 ^f	0.208	0.000	
	16436.624 _H	-0.116 ^a	-0.310	0.194	
	16679.164 _H	-0.690 ^a	-0.950	0.260	0.853

Continued next page

APPENDIX A. ASTROPHYSICAL GF-VALUES

χ_{exc} (eV)	λ (Å)	$\log(gf)_{VALD}$	$\log(gf)_{astph}$	$\Delta \log(gf)$	σ
5.931	11939.881 _J	-3.119 ^a	-1.470	-1.649	
5.943	15776.729 _H	-1.814 ^a	-1.780	-0.034	
5.946	13385.231 _J	-0.719 ^a	-1.650	0.931	
	15629.367 _H	-1.601 ^a	-1.800	0.199	
	15798.233 _H	-0.671 ^a	-0.700	0.029	
	15928.161 _H	-1.091 ^a	-0.720	-0.371	
	16506.296 _H	-0.335 ⁱ	-0.350	0.015	0.479
5.947	11743.695 _J	-1.759 ^a	-1.100	-0.659	
	11943.392 _J	-1.584 ^a	-1.070	-0.514	
	12131.180 _J	-1.274 ^a	-1.250	-0.024	
	15348.968 _H	-1.271 ^a	-0.916	-0.355	0.273
5.956	15224.731 _H	-0.331 ^a	-0.413	0.082	
	15816.633 _H	-0.500 ^a	-0.550	0.050	
	16070.183 _H	-0.625 ^a	-0.830	0.205	
	16156.560 _H	-0.308 ^a	-0.360	0.052	
	16454.904 _H	-1.068 ^a	-0.760	-0.308	
	16645.877 _H	-0.041 ⁱ	-0.080	0.039	0.172
5.979	15665.243 _H	-0.338 ^a	-0.440	0.102	
	15845.219 _H	-1.102 ^a	-1.310	0.208	
	16331.527 _H	-0.538 ^a	-0.480	-0.058	
	16561.767 _H	0.245 ⁱ	0.300	-0.055	
	16653.525 _H	-0.153 ⁱ	-0.240	0.087	0.114
6.017	12115.758 _J	-0.938 ^a	-1.620	0.682	
	16665.484 _H	-0.033 ^a	-0.080	0.047	
6.119	13289.688 _J	-1.743 ^a	-1.450	-0.293	
	13346.788 _J	-1.253 ^a	-1.440	0.187	
	14129.144 _H	0.328 ^a	0.370	-0.042	0.240
6.145	11572.006 _J	-1.405 ^a	-1.570	0.165	
	11989.548 _J	-0.895 ^a	-1.030	0.135	
	13209.764 _J	-1.341 ^a	-1.230	-0.111	0.151

Continued next page

APPENDIX A. ASTROPHYSICAL GF-VALUES

χ_{exc} (eV)	λ (Å)	$\log(gf)_{VALD}$	$\log(gf)_{astph}$	$\Delta \log(gf)$	σ
6.169	12283.299 _J	-0.541 ^a	-0.590	0.049	0.090
	14749.790 _H	0.599 ^a	0.760	-0.161	
	14979.698 _H	-0.450 ^a	-0.450	0.000	
	14988.781 _H	0.186 ^a	0.225	-0.039	
6.175	14205.601 _H	-0.007 ^a	-0.020	0.013	0.091
	14978.964 _H	-1.205 ^a	-1.054	-0.151	
	15305.374 _H	-1.274 ^a	-1.274	0.000	
6.200	14128.899 _H	-1.367 ^a	-0.091	-1.276	
6.206	14652.904 _H	0.508 ^a	0.603	-0.095	0.046
	15670.127 _H	-0.982 ^a	-0.970	-0.012	
	15894.755 _H	-0.582 ^a	-0.580	-0.002	
	16492.539 _H	-1.250 ⁱ	-1.250	0.000	
6.218	14158.181 _H	-0.295 ^a	-0.630	0.335	
6.222	12964.424 _J	-1.265 ^a	-1.310	0.045	0.510
	15013.773 _H	0.049 ^a	-0.328	0.377	
	15017.702 _H	0.056 ^a	-0.005	0.061	
	15095.860 _H	-0.860 ^a	0.110	-0.970	
	16864.082 _H	-1.538 ⁱ	-1.538	0.000	
6.237	14579.831 _H	-1.348 ^a	-1.106	-0.242	0.306
	14588.948 _H	-0.195 ^a	-0.578	0.383	
	14651.023 _H	0.405 ^a	0.412	-0.007	
	14654.401 _H	-0.851 ^a	-0.424	-0.427	
	15287.495 _H	-1.107 ^a	-1.330	0.223	
	16258.915 _H	-1.043 ^a	-0.830	-0.213	
6.242	14679.833 _H	-0.522 ^a	-0.150	-0.372	1.009
	15531.805 _H	-0.281 ^a	-1.420	1.139	
	15590.049 _H	-0.770 ^a	-0.420	-0.350	
	15604.223 _H	-1.044 ^a	0.610	-1.654	
	16227.154 _H	-1.740 ^a	-0.980	-0.760	
6.246	15652.874 _H	-0.170 ^a	-0.010	-0.160	
	15673.154 _H	0.650 ^a	-0.660	1.310	
	15677.015 _H	-0.112 ^a	-0.590	0.478	

Continued next page

APPENDIX A. ASTROPHYSICAL GF-VALUES

χ_{exc} (eV)	λ (Å)	$\log(gf)_{VALD}$	$\log(gf)_{astph}$	$\Delta \log(gf)$	σ
	15677.521 _H	-0.587 ^a	0.300	-0.887	
	15686.443 _H	0.581 ^a	0.250	0.331	
	15691.855 _H	-0.729 ^a	0.690	-1.419	0.986
6.252	14866.608 _H	-0.261 ^a	-0.640	0.379	
	15761.315 _H	-0.019 ^a	-0.019	0.000	
	15733.512 _H	-1.546 ^a	-0.650	-0.896	
	15788.998 _H	0.373 ^a	0.480	-0.107	
	15798.562 _H	0.047 ^a	0.530	-0.483	0.486
6.253	15681.397 _H	-1.326 ^a	-1.570	0.244	
6.258	14982.803 _H	-0.897 ^a	-0.502	-0.395	
	15863.712 _H	0.194 ^a	0.194	0.000	
	15895.228 _H	0.419 ^a	0.470	-0.051	
	15920.122 _H	-0.110 ^a	-0.910	0.800	
	15920.645 _H	0.001 ^a	0.440	-0.439	0.498
6.264	15080.223 _H	-0.613 ^a	-0.730	0.117	
	16037.821 _H	-0.581 ^a	0.280	-0.861	
	16051.736 _H	-0.766 ^a	-0.840	0.074	0.553
6.266	14105.432 _H	-0.977 ^a	-1.521	0.544	
	15112.333 _H	-1.056 ^a	-0.870	-0.186	
	16042.718 _H	0.330 ^a	0.290	0.040	
	16071.399 _H	0.109 ^a	0.109	0.000	
	16711.285 _H	-1.455 ^d	-2.300	0.845	
	15112.007 _H	-1.414 ^a	-1.414	0.000	0.397
6.268	12299.722 _J	-1.143 ^a	-1.240	0.097	
	14689.760 _H	0.100 ^a	-0.090	0.190	
	14842.706 _H	-0.570 ^a	-0.859	0.289	
	15015.465 _H	-1.013 ^a	-1.187	0.174	0.079
6.275	14641.659 _H	-0.738 ^a	-0.680	-0.058	
	15283.648 _H	-0.863 ^a	-1.006	0.143	
	15291.367 _H	-0.913 ^a	-0.806	-0.107	
	16180.903 _H	0.307 ^a	0.320	-0.013	
	16207.557 _H	-0.426 ^a	-2.426	2.000	
	16213.540 _H	0.276 ^a	0.240	0.036	

Continued next page

APPENDIX A. ASTROPHYSICAL GF-VALUES

χ_{exc} (eV)	λ (Å)	$\log(gf)_{VALD}$	$\log(gf)_{astph}$	$\Delta \log(gf)$	σ
	16243.068 _H	-0.909 ^a	-0.960	0.051	
	16246.462 _H	-0.045 ^a	-0.110	0.065	
	16272.470 _H	-1.817 ^a	-0.790	-1.027	0.788
6.277	14651.817 _H	-0.307 ^a	-0.162	-0.145	
	14968.329 _H	0.039 ^a	-0.030	0.069	
	15305.606 _H	-1.122 ^a	-0.645	-0.477	
	15387.806 _H	-1.657 ^a	-0.212	-1.445	
	15485.456 _H	-1.222 ^a	-0.832	-0.390	
	16087.165 _H	-0.726 ^a	-0.660	-0.066	
	16177.088 _H	-1.277 ^a	-1.040	-0.237	
	16410.390 _H	-1.239 ⁱ	-1.090	-0.149	0.473
6.280	11572.524 _J	0.322 ^a	0.320	0.002	
	11589.921 _J	-0.378 ^a	-0.371	-0.007	
	16316.371 _H	-1.208 ^a	-1.220	0.012	
	16396.309 _H	-2.447 ^d	-0.610	-1.837	0.920
6.286	15451.943 _H	-0.641 ^a	-0.994	0.353	
	15490.529 _H	-0.545 ^a	-2.545	2.000	
	15490.884 _H	-0.748 ^a	-0.547	-0.201	
	16407.789 _H	-0.006 ^f	-0.020	0.014	
	16440.397 _H	-0.254 ^a	-0.150	-0.104	
	16446.553 _H	-0.740 ^d	-1.740	1.000	
	16476.936 _H	-0.613 ^d	-0.530	-0.083	0.808
6.287	15501.323 _H	0.408 ^a	0.160	0.248	
	15514.282 _H	-0.384 ^a	-0.568	0.184	
	16494.705 _H	-0.640 ^d	-1.010	0.370	
	16517.226 _H	-0.951 ^a	0.760	-1.711	
	16521.514 _H	-0.753 ^a	-0.550	-0.203	
	16522.077 _H	0.286 ⁱ	0.000	0.286	
	16531.986 _H	-0.872 ⁱ	-0.000	-0.872	0.778
6.299	15099.106 _H	-1.267 ^a	-1.015	-0.252	
	15770.619 _H	0.448 ^a	0.448	0.000	
	15774.071 _H	0.529 ^a	0.520	0.009	
	16747.909 _H	-0.854 ^b	-1.040	0.186	
	16783.040 _H	-0.577 ^b	-0.810	0.233	
	16811.378 _H	-0.675 ⁱ	-0.730	0.055	0.171

Continued next page

APPENDIX A. ASTROPHYSICAL GF-VALUES

χ_{exc} (eV)	λ (Å)	$\log(gf)_{VALD}$	$\log(gf)_{astph}$	$\Delta \log(gf)$	σ
6.303	15819.134 _H	0.009 ^a	0.200	-0.191	0.396
	15829.298 _H	-1.241 ^a	-0.920	-0.321	
	15832.630 _H	-0.624 ^a	-0.780	0.156	
	15835.167 _H	0.738 ^a	0.870	-0.132	
	15837.646 _H	0.327 ^a	0.327	0.000	
	16900.234 _H	-0.494 ⁱ	-1.280	0.786	
6.306	15213.022 _H	-0.952 ^a	-0.766	-0.186	0.591
	15214.154 _H	-0.462 ^a	-1.188	0.726	
	15217.033 _H	-1.207 ^a	-1.907	0.700	
	15891.162 _H	0.069 ^a	-0.380	0.449	
	15892.398 _H	-0.025 ^a	0.420	-0.445	
	15897.657 _H	-0.745 ^a	-0.480	-0.265	
	15898.018 _H	-0.189 ^a	0.210	-0.399	
	15899.255 _H	0.246 ^a	-0.280	0.526	
	16893.783 _H	-0.835 ^d	-1.935	1.100	
	16900.283 _H	-0.778 ^d	-1.778	1.000	
6.308	14805.172 _H	-0.637 ^a	-0.895	0.258	0.151
	15260.644 _H	-0.537 ^a	-0.868	0.331	
	15929.475 _H	-0.391 ^a	-0.470	0.079	
	15934.020 _H	-0.302 ^a	-0.310	0.008	
6.311	15264.191 _H	-1.002 ^a	-1.079	0.077	0.055
	15293.138 _H	0.145 ^a	0.060	0.085	
	15645.018 _H	-0.352 ^a	-0.460	0.108	
	15837.079 _H	-0.993 ^a	-1.190	0.197	
6.319	16162.847 _H	-1.455 ^a	-1.060	-0.395	0.293
	16179.585 _H	0.260 ^a	0.200	0.060	
	16182.173 _H	-0.709 ^a	-0.860	0.151	
6.321	15476.503 _H	-0.734 ^a	-1.083	0.349	
	15479.606 _H	-0.214 ^a	-1.030	0.816	
	15500.801 _H	-0.010 ^a	-0.040	0.030	
	15571.751 _H	-1.162 ^a	-0.920	-0.242	
	16153.414 _H	-1.188 ^a	-1.188	0.000	
	16202.708 _H	-1.137 ^a	-1.480	0.343	
	16207.747 _H	0.544 ^a	0.590	-0.046	

Continued next page

APPENDIX A. ASTROPHYSICAL GF-VALUES

χ_{exc} (eV)	λ (Å)	$\log(gf)_{VALD}$	$\log(gf)_{astph}$	$\Delta \log(gf)$	σ
	16213.004 _H	-0.440 ^a	-0.440	0.000	
	15522.609 _H	-0.921 ^a	-0.921	0.000	0.315
6.323	15521.684 _H	-1.222 ^a	-1.378	0.156	
	15537.697 _H	-0.031 ^a	-0.250	0.219	
	15550.439 _H	-0.145 ^a	-0.270	0.125	
	15565.225 _H	-0.570 ^a	-0.810	0.240	
	15579.080 _H	-1.854 ^a	-0.910	-0.944	
	16203.331 _H	-0.879 ^a	-0.670	-0.209	
	16240.872 _H	-0.221 ^a	-0.830	0.609	
	16245.765 _H	-1.782 ^a	-0.660	-1.122	
	16252.553 _H	-0.329 ^a	-0.420	0.091	0.575
6.325	11727.734 _J	-1.011 ^a	-1.021	0.010	
	12331.017 _J	-1.332 ^a	-1.140	-0.192	
6.329	14931.854 _H	-0.890 ^a	-1.020	0.130	
	15182.927 _H	-0.610 ^a	-0.660	0.050	
	15671.006 _H	-0.282 ^a	-0.510	0.228	
	15686.022 _H	-0.028 ^a	-0.100	0.072	0.080
6.333	11789.650 _J	-1.175 ^a	-1.350	0.175	
	11920.116 _J	-2.251 ^a	-0.950	-1.301	
	13302.294 _J	-1.238 ^a	-0.980	-0.258	
	13303.831 _J	-1.287 ^a	-1.340	0.053	0.671
6.336	15781.665 _H	-0.885 ^a	-1.830	0.945	
	15806.278 _H	0.063 ^a	-0.640	0.703	
	16539.196 _H	-0.145 ^a	-0.100	-0.045	
	16540.873 _H	-0.663 ^a	-0.700	0.037	
	16541.965 _H	0.162 ⁱ	-0.310	0.472	
	16544.670 _H	-0.025 ^a	-0.300	0.275	0.385
6.342	15160.506 _H	-0.211 ^a	-0.308	0.097	
	15160.834 _H	-1.193 ^a	-0.953	-0.240	
	15395.875 _H	-1.363 ^a	-1.350	-0.013	
	15892.456 _H	-0.145 ^a	-0.145	0.000	
	15896.557 _H	0.257 ^a	-0.890	1.147	
	15909.087 _H	0.059 ^a	-0.890	0.949	
	15909.244 _H	-0.491 ^a	-0.630	0.139	

Continued next page

APPENDIX A. ASTROPHYSICAL GF-VALUES

χ_{exc} (eV)	λ (Å)	$\log(gf)_{VALD}$	$\log(gf)_{astph}$	$\Delta \log(gf)$	σ
	15922.445 _H	-0.674 ^a	-1.374	0.700	
	15922.602 _H	-0.635 ^a	-1.435	0.800	
	15938.105 _H	-0.876 ^a	-0.940	0.064	
	16607.808 _H	-0.858 ⁱ	-1.858	1.000	
	16652.218 _H	-0.800 ^d	-0.560	-0.240	
	16652.390 _H	-0.412 ^a	-1.912	1.500	
	16661.382 _H	-0.501 ⁱ	0.160	-0.661	0.634
6.347	15502.176 _H	-1.236 ^a	-1.045	-0.191	
	15551.435 _H	-0.383 ^a	-0.200	-0.183	
	16007.086 _H	0.216 ^a	0.160	0.056	
	16019.790 _H	-0.592 ^a	-0.690	0.098	
	16029.425 _H	-1.643 ^a	-0.540	-1.103	
	16782.843 _H	-0.839 ^a	-1.839	1.000	
	16786.588 _H	-0.414 ^c	-0.970	0.556	
	16792.227 _H	-1.083 ^d	-0.950	-0.133	0.612
6.349	15297.170 _H	-0.915 ^a	-0.986	0.071	
	15560.786 _H	-0.487 ^a	-0.470	-0.017	
	16073.872 _H	-0.579 ^a	-0.579	0.000	
	16089.671 _H	-0.556 ^a	-0.750	0.194	0.096
6.350	15323.557 _H	-0.657 ^a	-0.807	0.150	
	15566.727 _H	-0.428 ^a	-0.410	-0.018	
	15613.628 _H	-0.517 ^a	-0.100	-0.417	
	16071.565 _H	-0.209 ^a	-1.420	1.211	
	16088.733 _H	-1.512 ^a	-0.050	-1.462	
	15591.306 _H	-1.401 ^a	-1.401	0.000	0.866
6.352	16100.284 _H	-0.060 ^a	-0.050	-0.010	
	16100.614 _H	-0.970 ^a	-0.970	0.000	
	16123.215 _H	-0.519 ^a	-1.020	0.501	
	16874.119 _H	-0.151 ^f	-0.820	0.669	0.348
6.360	14620.103 _H	-0.038 ^a	-0.302	0.264	
	15751.717 _H	-0.979 ^a	-0.979	0.000	
	15941.851 _H	0.272 ^a	0.060	0.212	
	15094.697 _H	0.599 ^a	0.599	0.000	0.139
6.364	15591.500 _H	-0.570 ^a	-0.570	0.000	

Continued next page

APPENDIX A. ASTROPHYSICAL GF-VALUES

χ_{exc} (eV)	λ (Å)	$\log(gf)_{VALD}$	$\log(gf)_{astph}$	$\Delta \log(gf)$	σ
	15864.649 _H	-0.747 ^a	-0.640	-0.107	
	15868.574 _H	0.405 ^a	-0.800	1.205	
	16384.144 _H	-0.582 ^a	-0.200	-0.382	
	16398.312 _H	-0.587 ^a	-0.587	0.000	
	16414.755 _H	-1.085 ^a	-1.085	0.000	0.552
6.365	15901.452 _H	-0.928 ^a	-0.928	0.000	
	16377.391 _H	-0.482 ^a	-0.250	-0.232	
	16404.604 _H	0.565 ^a	0.630	-0.065	0.120
6.367	14959.222 _H	0.065 ^a	0.050	0.015	
	15588.262 _H	0.435 ^a	0.400	0.035	
6.369	15682.516 _H	-0.137 ^a	-0.330	0.193	
	15938.920 _H	0.070 ^a	-0.330	0.400	
	15967.657 _H	-0.648 ^a	0.350	-0.998	
	16471.756 _H	-0.054 ⁱ	-0.610	0.556	0.706
6.380	16171.933 _H	-0.454 ^a	-0.440	-0.014	
	16174.978 _H	0.176 ^a	0.300	-0.124	
	16201.516 _H	-0.331 ^a	-0.530	0.199	
	16225.621 _H	0.292 ^a	0.150	0.142	
	16720.730 _H	-0.806 ⁱ	-0.770	-0.036	
	16721.465 _H	-0.520 ^a	-0.430	-0.090	
	16725.443 _H	-0.597 ⁱ	-0.860	0.263	
	16739.314 _H	-0.850 ^a	-0.850	0.000	0.141
6.381	16177.994 _H	-0.423 ^a	-0.470	0.047	
	16228.655 _H	-0.905 ^a	-1.140	0.235	
	16231.649 _H	0.580 ^a	0.660	-0.080	
	16724.688 _H	-0.416 ⁱ	-0.660	0.244	
	16728.312 _H	-0.786 ⁱ	-1.060	0.274	
	16753.068 _H	0.407 ^a	0.290	0.117	0.138
6.390	16115.142 _H	-0.404 ^a	-0.540	0.136	
	16115.969 _H	0.426 ^a	0.390	0.036	
	16412.174 _H	-0.908 ⁱ	-0.860	-0.048	0.092
6.394	16185.802 _H	0.268 ^a	0.230	0.038	
	16195.063 _H	0.464 ^a	0.270	0.194	

Continued next page

APPENDIX A. ASTROPHYSICAL GF-VALUES

χ_{exc} (eV)	λ (Å)	$\log(gf)_{VALD}$	$\log(gf)_{astph}$	$\Delta \log(gf)$	σ
	16466.924 _H	-0.007 ⁱ	0.160	-0.167	
	16481.231 _H	-0.163 ⁱ	-0.310	0.147	
	16494.430 _H	-0.532 ^a	-0.470	-0.062	0.148
6.398	16284.772 _H	-0.230 ^a	0.210	-0.440	
	16559.680 _H	0.192 ⁱ	-0.250	0.442	
	16612.764 _H	0.280 ⁱ	0.040	0.240	0.462
6.411	16551.997 _H	0.321 ^a	0.120	0.201	
	16557.151 _H	-1.161 ^a	-0.410	-0.751	
	16837.880 _H	-0.416 ^a	-0.380	-0.036	
	16865.516 _H	-0.759 ^a	-0.880	0.121	
	16869.953 _H	-0.394 ^a	-1.100	0.706	0.526
6.415	15294.904 _H	-0.082 ^a	-0.181	0.099	
	15639.480 _H	-0.056 ^a	-0.820	0.764	
	15971.251 _H	-0.139 ^a	-0.310	0.171	0.365
6.417	16693.075 _H	-0.158 ^d	-0.330	0.172	
6.419	14480.606 _H	0.020 ^a	0.060	-0.040	
	14897.408 _H	0.045 ^a	0.330	-0.285	
	15239.715 _H	-0.004 ^a	-0.067	0.063	
	15962.560 _H	-0.076 ^a	-0.016	-0.060	0.147
6.441	12217.433 _J	-0.785 ^a	-0.940	0.155	
6.452	15427.621 _H	-0.784 ^a	-0.947	0.163	
	15731.415 _H	-0.291 ^a	-0.630	0.339	
6.453	14169.523 _H	-0.374 ^a	-0.260	-0.114	
	14463.279 _H	-0.554 ^a	-1.047	0.493	
	14903.935 _H	0.106 ^a	0.070	0.036	
	15451.301 _H	-0.213 ^a	-0.435	0.222	
	15917.332 _H	-0.394 ^a	-0.510	0.116	0.227
6.456	14943.246 _H	-2.056 ^a	-0.481	-1.575	
6.474	14781.956 _H	-0.482 ^a	-0.500	0.018	
	15854.444 _H	-0.875 ^a	-0.723	-0.152	

Continued next page

APPENDIX A. ASTROPHYSICAL GF-VALUES

χ_{exc} (eV)	λ (Å)	$\log(gf)_{VALD}$	$\log(gf)_{astph}$	$\Delta \log(gf)$	σ
	16345.497 _H	-0.787 ^a	-0.840	0.053	0.110
6.479	14075.004 _H	-0.807 ^a	-0.710	-0.097	
	15963.302 _H	-0.942 ^a	-1.130	0.188	
6.547	16648.203 _H	-0.250 ^f	-0.450	0.200	
6.565	16794.210 _H	-0.441 ^a	-0.320	-0.121	
6.606	16711.598 _H	-1.042 ^a	-1.130	0.088	
6.616	16570.511 _H	-0.820 ^{g,h}	-1.250	0.430	

^a Kurucz (2007), ^b Kurucz (2006), ^cKurucz (1988), ^dKurucz & Peytremann (1975), ^eO'Brian et al. (1991), ^fRaassen & Uylings (1998), ^gBiemont et al. (1999), ^hQuinet & Biemont (2004), ⁱ no reference given.

Appendix B

SME Jobs for Temperature Uncertainties

Table B.1: Temperature-measurements for the different linelists obtained when adding Gaussian noise in gf-values assuming a standard deviation of $\sigma = 0.02$ dex.

$T_i(70\text{-Felist})$	$T_i(80\text{-Felist})$	$T_i(95\text{-Felist})$
4306	4303	4245
4258	4293	4208
4256	4270	4188
4291	4265	4220
4260	4256	4258
4285	4293	4245
4297	4149	4185
4279	4176	4188
4263	4193	4169
4250	4199	4233
4248	4167	4177
4250	4252	4177
4237	4185	4282
4269	4154	4221
4315	4177	4173
4154	4170	4183
4197	4201	4213
4219	4248	4190
4203	4229	4231
4234	4263	4250
4260	4267	4180